27th Conf. on Weather Analysis and Forecasting
23rd Conf. on Numerical Weather Prediction
Chicago, IL, Amer. Met. Soc., 2015

13A.6 VERIFICATION OF 24 MAY 2011 SIMULATED MESOCYCLONES USING VARIOUS MICROPHYSICS SCHEMES AT 1-KM GRID RESOLUTION

Derek R. Stratman[1,2] * and Keith A. Brewster[1]
[1]Center for Analysis and Prediction of Storms, Norman, Oklahoma
[2]School of Meteorology, University of Oklahoma, Norman, Oklahoma

1. INTRODUCTION

On the afternoon of 24 May 2011, an outbreak of twelve tornadoes, including two EF-4 tornadoes and one EF-5 tornado, blitzed northern and central Oklahoma within the Norman, OK, National Weather Service (NWS) Weather Forecast Office's county warning area. This outbreak caused 11 deaths and 293 injuries (see http://www.srh.noaa.gov/oun/?n=events-20110524 for more information). An extensive observation network was in place in this area during the spring of 2011, so despite the tragic loss of life, this is an ideal case to explore the Warn-on-Forecast (WoF) concept (Stensrud et al., 2009, 2013) with storm-scale numerical simulations.

The tight clustering of the tornadic and non-tornadic supercells on this date made forecasting of storm tracks difficult for storm-scale models, but the Center for Analysis and Prediction of Storms (CAPS) real-time forecasting system had good success at simulating these storms. However, improvements in storm tracks and timing might be expected using more sophisticated microphysics schemes or an ensemble of simulations with microphysics diversity. Therefore, this study examines the impact of using five different microphysics parameterization schemes (Table 1) on the genesis and evolution of simulated mesocyclones (MC) and uses a potential future WoF framework to explore the WoF concept on a real-world case with complex storm morphologies and interactions.

Instead of using vertical vorticity to identify and track MC centers (as in, e.g., Trapp and Weisman, 2003 and Schenkman et al., 2011), updraft helicity (UH; Kain et al., 2008, which used UH from 2 to 5 km AGL) is used because UH is the integral of the product of vertical vorticity and vertical velocity through a designated depth. The UH centers are compared to each other and reality via estimated tornado point locations. Similar to hurricane center errors (e.g., Xue et al., 2013), UH center distance and timing errors are computed to assess model performance.

Recently, the Advanced Regional Prediction System's (ARPS; Xue et al., 2000; Xue et al., 2001; Xue et al., 2003) data assimilation system's (ADAS) complex cloud analysis package (Hu et al., 2006a,b) was updated for several microphysics schemes, including the five in this study (Brewster and Stratman, 2015). The goal of this update was to improve analyses of hydrometeors using scheme-specific reflectivity inversion equations.

The numerical simulation methodology for this study, including details about the observational data and model settings, are described in section 2. The verification methodology is described in section 3. Results of the numerical simulations and their verification are presented in section 4. Lastly, section 5 will provide a summary and discussion of the results, along with potential future work.

2. SIMULATION METHODOLOGY

Since this experiment intends to explore the capabilities of the forecast system in a realistic setting, the numerical simulations use data from multiple observing platforms. Surface observations from NWS and FAA METAR and Oklahoma Mesonet stations along with radial wind and reflectivity data from the WSR-88D [Dallas/Fort Worth (KFWS), Dodge City (KDDC), Frederick (KFDR), Tulsa (KINX), Twin Lakes (KTLX), Vance (KVNX), and Wichita (KICT)] and Collaborative Adaptive Sensing of the Atmosphere (CASA) IP-1 [Chickasha (KSAO), Cyril (KCYR), Lawton (KLWE), and Rush Springs (KRSP); see Fig. 1] radar networks (McLaughlin et al., 2009) are ingested into the initial analyses of the numerical simulations.

The 1800 UTC 12-km NAM (North American Mesoscale) model's 3-hour forecast is used as a background field in CAPS' ARPS's three-dimensional variational (3DVAR; Gao et al., 2004) and complex cloud analysis data assimilation process to produce an initial analysis on a 323x353-km domain with 1-km horizontal grid spacing (Fig. 1) and 53 vertically-stretched levels with a minimum vertical grid spacing of 20 m at the bottom. Three analysis passes with 20, 50, and 50 iterations and horizontal influence radii of 45, 2, and 1 km, respectively, are used to produce the 3DVAR analysis through the minimization of the cost function. The surface in-situ data is implemented in the first and third passes, while the radar data is applied in the

* *Corresponding author address:* Derek R. Stratman, The Univ. of Oklahoma, School of Meteorology, Norman, OK 73072; e-mail: stratman@ou.edu

second and third passes. In addition, a 3D mass divergence constraint is utilized to couple the wind components together (Hu et al., 2006b).

After the 3DVAR analysis is produced, an ARPS model simulation is integrated to produce forecasts out to 125 minutes. During the first 5 min, an incremental analysis update (IAU, Bloom et al., 1996) is performed by introducing the analysis increments every 20 s. The increments are applied to all fields except for vertical velocity and pressure since those two fields are not directly observed in 3D and will quickly respond to the other fields to create a balanced state. The simulation proceeds on its own for the remaining 120 min.

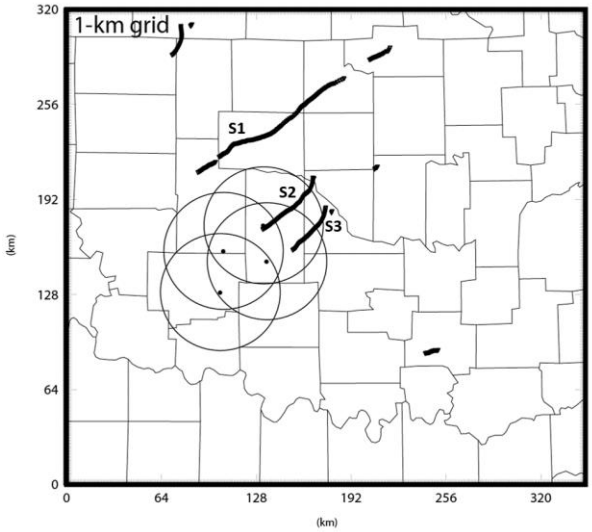

Figure 1. Domain of numerical simulations with CASA radar locations and 40-km range rings, estimated tornado points, and storm IDs.

During the integration of ARPS, a big and small time step of 2.0 s and 0.5 s, respectively, are employed in the leapfrog time formulation. In addition, the 1800 UTC 12-km NAM forecasts are used for the lateral boundary conditions. Some other model details include: 4th-order momentum advection in both the horizontal and vertical directions, scalar advection using Zalesak's multi-dimensional version of flux-corrected transport (Zalesak, 1979), 1.5-order TKE closure based on Sun and Chang (1986), 4th-order computational mixing, Rayleigh damping beginning at 12-km AGL, National Aeronautics and Space Administration atmospheric radiation transfer parameterization, surface fluxes calculated from stability-dependent surface drag coefficients using predicted surface temperature and volumetric water content, and two-layer force-store soil model based on Noilhan and Planton (1989). The modeling process is summarized with a flow chart in Figure 2.

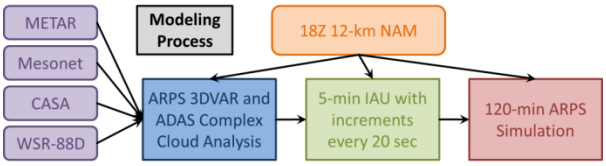

Figure 2. Flow chart of the modeling process used in this numerical simulation experiment.

Research experiments are done using five different microphysics parameterization schemes: Lin 3-ice microphysics scheme (Lin et al., 1983), Weather Research and Forecasting (WRF) single-moment 6-class microphysics scheme (Hong and Lim, 2006), Milbrandt and Yau (MY) single-moment bulk microphysics scheme, MY double-moment bulk microphysics scheme, and MY triple-moment bulk microphysics scheme (Milbrandt and Yau 2005a,b; Table 1).

ID	Microphysics Scheme
LIN3	Lin 3-ice microphysics
WSM6	Weather Research and Forecasting single-moment 6-class microphysics
MYSM	Milbrandt and Yau (MY) single-moment bulk microphysics
MYDM	MY double-moment bulk microphysics
MYTM	MY triple-moment bulk microphysics

Table 1. List of microphysics schemes used in the numerical simulations with their associated ID names.

In addition to microphysics diversity, simulations are run using a potential future WoF framework. Eight simulations are integrated every 30 minutes starting at 1900 UTC (IAU begins at 1855 UTC) and ending at 2230 UTC (Table 2). With this WoF framework, tornado genesis (dissipation) for each of the storms of interest is captured by four (at least one) simulations. The first storm (S1; storms depicted in Fig. 1) developed and stayed outside the CASA radar network and produced two tornadoes, including the outbreak's only EF-5 tornado. The second and third storms (S2 and S3, respectively) developed in the CASA radar network and both produced EF-4 tornadoes, which dissipated before impacting the Oklahoma City metro area.

ARPS Begin – End	S1 2031 Z - 2046 Z 2050 Z - 2235 Z 2250 Z - 2305 Z	S2 2206 Z - 2301 Z	S3 2226 Z - 2305 Z 2302 Z - 2303 Z
1900 Z – 2100 Z	+1:31		
1930 Z – 2130 Z	+1:01		
2000 Z – 2200 Z	+0:31		
2030 Z – 2230 Z	+0:01	+1:36	+1:56
2100 Z – 2300 Z	-0:29	+1:06	+1:26
2130 Z – 2330 Z	-0:59	+0:36	+0:56
2200 Z – 0000 Z	-1:29	+0:06	+0:26
2230 Z – 0030 Z	-1:59	-0:24	-0:04

Table 2. List of storm ID names and associated tornado and ARPS-simulation forecast times. Positive (green) and negative (red) values indicate the time difference between the start of the simulations and first tornadogenesis for each of the storms.

3. VERIFICATION METHODOLOGY

To assess model performance, simulated MC centers via the UH field are compared to each other and verified using estimated tornado points. The locations of the six tornadoes associated with the three storms of interest are estimated every minute based on NWS damage surveys, radar data, and high-resolution aerial photos from Google Maps. Two adjacent layers of UH (namely, 1–6 km and 0–1 km) are used for the verification of the simulations. These two layers are intended to represent simulated mid-level and low-level mesocyclones, respectively. As mentioned before, Kain et al. (2008) used UH from 2 to 5 km AGL to signify mid-level mesocyclones, but for this study, a deeper layer of UH is utilized to give more robust UH values by capturing more of the simulated mid-level MCs.

Since UH is a 2D field and not point data, a simple 2D object-based technique is utilized to find UH-weighted centers (analogous to mass-weighted centers), which will be compared to the estimated tornado points. A search radius of 10 km (i.e., 10 grid points) is used to isolate 1–6-km (0–1-km) UH maxima that are greater than or equal to 800 $m^2 s^{-2}$ (40 $m^2 s^{-2}$) and their surrounding grid point values. A max UH value is considered a UH-center candidate if 7 out of 8 (4 out of 8) of the adjacent grid point values equals or exceeds 400 $m^2 s^{-2}$ (20 $m^2 s^{-2}$). Once the UH-center candidates are determined, the UH-weighted center is computed using a radius of 5 km extending from the grid point with the max UH value.

With the UH-weighted center locations, an objective verification technique is used to quantify location and timing errors. First, distance errors are computed between the estimated tornado point locations and the nearest UH center locations at coincident times (referred to as “same time”, or ST, for rest of paper). Second, distance and timing errors are calculated between the estimated tornado point locations and the nearest UH center locations at any occurrence time (referred to as “any time”, or AT, for rest of paper).

4. RESULTS

4.1 *Simulations Overview*

Before presenting the quantitative verification, a subjective comparison of UH center locations for each set of simulations is provided as an informative overview similar to how a forecaster may view the forecast output. In Figure 3, 1–6-km UH (1-6UH; a, c, e, g, i, k, m, and o) and 0–1-km UH (0-1UH; b, d, f, h, j, l, n, and p) centers for the five microphysically-different simulations are plotted using forecasts from every five minutes. Additionally, estimated tornado points from the entire tornado outbreak are plotted for every minute, and tornado points highlighted in black indicate which tornado points occur at the same times as the forecast output. These highlighted tornado points are used in the ST distance error computations.

For the 1900 UTC simulations, the runs with WSM6, MYSM, MYDM, and MYTM all performed very well in capturing the location of the S1 tornado points, but LIN3’s UH centers ended up too far south (Fig. 3a,b). As might be expected with supercell dynamics, the 0-1UH centers are slightly further south of the 1-6UH centers, so the MY schemes’ 0-1UH centers are closer to the tornado points while LIN3 and WSM6’s 0-1UH centers are further away than their 1-6UH centers. The 1930 UTC simulations have UH centers too far north, especially for the second part of S1’s path (Fig. 3c,d). Also, the existence of UH centers further east than the estimated tornado points indicates the simulated rotating storms are propagating too fast.

Similar to the 1900 UTC simulations, the MY schemes for the 2000 UTC simulations performed well for S1, while LIN3 and WSM6 are too far south of the tornado points (Fig. 3e,f). UH centers associated with S2 and S3 appear for the first time, as well. Even though most of S1’s tornado points occur during the 2030 UTC simulations, the simulations fail to produce long-track rotating storms near S1’s path (Fig. 3g,h). There are some UH centers near the beginning of S2’s tornado points, but nothing near S3’s tornado points.

For the 2100 UTC simulations, LIN3 and WSM6 both have UH centers near S1’s tornado points, while the MY schemes are too far north (Fig. 3i,j). Only a few UH centers exist near S2 and S3’s tornado points. For the 2130 UTC simulations, the MY schemes perform poorly for the first half of S1, but they perform better for the end of S1’s second tornado (Fig. 3k,l). All microphysics schemes have several UH-center tracks between S1 and S2, but the UH centers remain north of

S2's tornado points. Also, the simulations at this initialization time fail at forecasting S3.

The 2200 UTC simulations somewhat capture S1's second tornado, but the UH-center tracks diverge to the north of S1's third tornado (Fig. 3m,n). Some UH centers exist near the end of S2's tornado path, but the majority of the UH centers occur too far to the east. Once again, the simulations fail at forecasting S3. For the 2230 UTC simulations, only a few UH centers occur near any of the storms' tornado points (Fig. 3o,p). Several UH centers are forecasted for the eastern part of the model domain even though no observed tornadoes occurred in that area. However, the simulations may have been picking up on real-life, non-tornadic rotating supercells, so the forecasts may still have some merit since a 1-km model is too coarse to simulate actual tornadoes.

4.2 *Storm 1*

For S1, all, except for LIN3, of the 1900 UTC simulations' UH centers have remarkably small (<5 km) ST distance errors (Fig. 4a,b). The quantitative AT distance and timing errors are larger simply due to UH centers existing prior to S1's first tornado (Fig 4c,d). For the 1930 UTC simulations, the UH centers are somewhat fast and generally displaced slightly to the north, except for LIN3 (Fig. 5). With the 2000 UTC simulations, the UH centers are more evenly distributed north and south of the tornado points while being a little too fast, but the LIN3 and WSM6 schemes' centers are mostly biased south (Fig. 6). The 2030 UTC simulations produce a scattering of UH centers around the tornado points (Fig. 7a,b), but the AT distance errors indicate most of the UH centers occur near the tornado points (Fig. 7c,d).

The 2100 UTC simulations depict similar results with a scattering of UH centers in most directions from the tornado centers (Fig. 8a,b), but the AT plots reveal most of the UH centers are placed within 10 km north of the tornado points (Fig. 8c,d). The scattering of UH centers is more clustered near the tornado points in the 2130 UTC simulations (Fig. 9a,b), and the MY schemes tend to produce more UH centers near the tornado points than LIN3 and WSM6 (Fig. 9c,d). For the 2200 UTC simulations, the MY schemes have a cluster of UH centers near the tornado points while LIN3 has ST and AT distance errors more than two times the errors from the other schemes (Fig. 10). Very few UH centers exist near the tornado points from the 2230 UTC simulations indicating reduced model performance compared to earlier simulations (Fig. 11).

To summarize the model successes and failures, average distance and timing errors are plotted to add a new dimension of verification. ST distance errors for both 1-6UH and 0-1UH indicate the MY schemes generally performed better than LIN3 and WSM6 before and after the first tornadogenesis (Fig. 12a,b). AT distance errors for 1-6UH slightly decrease prior to tornadogenesis and then slowly increase after the first tornadogenesis (Fig. 12c). These trends are less evident for 0-1UH (Fig. 12d). The MY schemes tend to have lower average AT distance errors than LIN3 and WSM6 for 0-1UH (Fig. 12d), but for 1-6UH, the difference in average AT distance errors is negligible (Fig. 12c). A downward trend from positive to negative (i.e., too fast to too slow) average AT timing errors occurs for all of the schemes, but the MY schemes cross the zero error line closer to the first tornadogenesis than LIN3 and WSM6 (Fig. 12e,f).

4.3 *Storm 2*

Even though the 2000 UTC simulations don't overlap with S2's tornadogenesis, the 2000 UTC simulations do produce UH centers within about 20 km north and south of S2's tornado points, and while LIN3 has the smallest AT distance errors, it also has the largest AT timing errors (Fig. 13a,b). For the 2030 UTC simulations, very few UH centers occur concurrently near S2's tornado points (Fig. 14a,b), but for AT errors, a plethora of UH centers generally exist along and to the north of the S2 tornado path (Fig. 14c,d). The 2100 UTC simulations perform worse with no UH centers within 10 km of the tornado points (Fig. 15a,b), but several UH centers do occur at some point during the life of the tornado, mainly to the north of the average tornado track (Fig. 15c,d).

The MY schemes from the 2130 UTC simulations perform better than LIN3 and WSM6 for both ST and AT distance and timing errors with a majority of their UH centers falling within 20 km of the tornado points (Fig. 16). For the 2200 UTC simulations, all of the schemes produce UH centers within 20 km of the tornado locations, but the UH centers are, on average, too fast (Fig. 17). The 2230 UTC simulations produce a small cluster of UH centers about 15 km from the tornado points, but the UH centers are too slow (Fig. 18).

As viewed in a graph (Fig. 19a,b), LIN3 and WSM6 have similar ST distance errors, which are mostly larger than the MY schemes' ST distance errors, but LIN3 and WSM6 are more consistent from run to run with an obvious downward trend. Smaller differences exist among the schemes for AT distance errors, with LIN3 and WSM6 performing better than the MY schemes for some initialization times (Fig. 19c,d). Once again, timing errors form a downward trend from positive to negative values with a zero-line crossover occurring as early as the 2130 UTC simulations for some of the schemes (Fig. 19e,f).

4.4 *Storm 3*

Similar to S2, the 2000 UTC simulations for LIN3 and WSM6 produce UH centers more than 30 minutes too early and not within 10 km of the tornado points (Fig. 20 a,b). For the 2030 UTC simulations only MYSM indicates a UH center within the interested range (Fig. 21 a,b). A few more UH centers from LIN3, WSM6, and MYSM show up in the AT plots, but either the distance or timing errors are too large to consider their storm rotation forecasts to be successful (Fig. 21 c,d). No ST 1-6UH centers exist within the designated range for the 2100 UTC simulations, but a couple of 0-1UH centers fall outside 10 km of the tornado points (Fig. 22a,b). Several UH centers exist south of the tornado points, but the AT distance errors are fairly large (Fig. 22c,d).

For the 2130 UTC simulations, LIN3 and the MY schemes produce UH centers concurrent with the tornado points, but due to timing errors ST distance errors are greater than 30 km (Fig. 23a,b). WSM6 has the smallest AT distance errors with all schemes having timing errors less than 20 minutes (Fig. 23c,d). No 1-6UH centers exist within 30 km of the tornado points for the 2200 UTC simulations, but the MY schemes do have some 0-1UH centers within 10 km of the tornado points (Fig. 24a,b). Similarly, AT distance errors are smaller for 0-1UH than 1-6UH, and timing errors vary widely with most UH centers occurring too late (Fig. 24c,d). For the 2230 UTC simulations, a couple of 1-6UH centers from WSM6 and the MY schemes reside within about 5 km of the tornado points, but that small success is overshadowed by UH centers further away (Fig. 25).

Due to the lack of UH centers concurrent with the tornado points, the ST distance errors vary widely from run to run and among the microphysics schemes (Fig. 26a,b). Even though some UH centers exist near the tornado points, the majority of the average AT distance errors are greater than 20 km due to a large number of UH centers showing up more than 30 km to the south but within the interested range (Fig. 26c,d). As in S1 and S2, a downward trend in timing errors with a crossover from positive to negative values occurs one or two model runs prior to S3's first tornadogenesis (Fig. 26e,f).

5. SUMMARY AND DISCUSSION

On 24 May 2011, a tornado outbreak affected parts of central Oklahoma. For this study, three storms with violent tornadoes from this outbreak are used to evaluate the performance of a microphysically-diverse set of simulations in a potential WoF setting. The evaluation of simulated MCs using the UH field compared to estimated actual tornado locations has proven to be an effective measure of model skill. The verification technique applied in the evaluation process highlights these model successes and failures and helps define expected error bounds when utilizing microphysics diversity for the WoF ensemble concept (though any operational WoF setup will have a much larger ensemble size).

It is remarkable that the science of data assimilation and NWP has advanced to the point that we can actually compare actual tornado locations to NWP forecasts of storm rotation from an analysis and modeling system that can run in real-time with low latency on today's computers. CAPS is currently running an NWP system similar to the one examined here in the Dallas-Fort Worth Testbed on 192 processing cores with latency less than 10-min (Brewster and Stratman, 2015). With additional cores a microphysics-diverse ensemble could be run with the same latency.

Forecasting a complex real-world case yielded variations in model skill. The environment certainly was well forecasted to support several tornadic storms, but getting the details of storm rotation close-to-right is more difficult when multiple storms occur within close proximity to each other. The MY schemes tend to perform better, but all schemes had more difficulty predicting the rotation centers with S2 and especially with S3. This result suggests that more model forecasting successes happen with fewer, well-spaced storms, and it'd be wise for researchers to study cases beyond isolated supercells.

An interesting result from this study is that while S2 and S3 both develop within the CASA radar network they are both poorly forecasted as compared to the forecasting of S1. This is not to say the CASA radar data had no impact on the successful forecasts of S1, but perhaps the potential benefit of using CASA radar data in the assimilation process is more evident in less convectively active conditions in contrast to the conclusions drawn from some previous work (e.g., Schenkman et al., 2011).

In several forecasts, the UH centers tend to be too far north and too fast. This finding is not unique to this study as it has been found by other studies (e.g., Xue et al., 2014 and Potvin et al., 2014). Furthermore, 0-1UH centers are typically further south than the 1-6UH centers, so when the UH centers are too far north, the 0-1UH centers are closer to the estimated tornado points than the 1-6UH centers.

Regarding the WoF ensemble forecasting concept, the locations of UH tracks sometimes aren't substantially dissimilar among the tested simulations, but some potentially useful ensemble spread is evident in both the subjective and objective evaluations, especially after the first 15 min following the end of the 5-min IAU. The MY schemes' UH centers tended to cluster together in most, less-noisy forecasts (i.e., less spread when fewer storms), so this might imply that using a single MY scheme in an ensemble would be

sufficient and more spread might be gained by adding another microphysics scheme to the mix.

Minimums in average distance errors from forecasts initialized prior to tornadogenesis might indicate the optimal time for simulations to be initialized, but since this study only focuses on three storms from the same tornado outbreak, no conclusions can be drawn yet. Even though there are no common trends in the average distance errors, the average timing errors do exhibit a trend from being too fast to being too slow. This might be due to the increase in the number of simulated storms developing later in the simulations near the tornado points after the initial wave of convection moves to the east (i.e., a second wave of convection).

Some potential future work might include the exploration of other variables (e.g., vertical vorticity, vertical wind, and horizontal wind) for verification using the simple object-based, center-tracking method developed for this study. Furthermore, application of this verification technique using the Storm Prediction Center's storm reports database instead of estimated tornado points could be used to verify a wide range of different severe storm episodes. Taking model verification one step further, the investigation into whether a model's analysis (e.g., 3DVAR/IAU analysis) can be used in place of estimated tornado points or storm reports for the verification of a model's forecast may be worth considering since any model field can then be verified with the same field from a real-time analysis.

As previously mentioned, the ADAS complex cloud analysis package was updated to be more compliant with a range of cloud and precipitation microphysics schemes, and while substantial improvements were made in the initial analyses (Brewster and Stratman, 2015), additional modifications could be made for further improvements. Due to the failures of forecasting S2 and S3, further work might be directed at addressing the impact of assimilating CASA radar data in the initial analyses for all three simulated storms. No cycling was used in this study, but perhaps cycling could be employed to potentially improve forecasts, especially for S2 and S3.

ACKNOWLEDGEMENTS

This work is supported by the National Science Foundation via CASA ERC grant EEC 03-13747 and related support provided by the University of Oklahoma (OU). Any opinions, findings, and conclusions or recommendations expressed in this material are those of the authors and do not necessarily reflect the views of the National Science Foundation. Most of the computing for this project was performed at the OU Supercomputing Center for Education & Research (OSCER). This work utilized data from the Oklahoma Mesonet provided by the Oklahoma Climatological Survey.

REFERENCES

Bloom, S. C., L. L. Takacs, A. M. da Silva, and D. Ledvina, 1996: Data Assimilation Using Incremental Analysis Updates. *Mon. Wea. Rev.*, 124, 1256–1271.

Brewster, K. A. and D. R. Stratman, 2015: An Updated High Resolution Hydrometeor Analysis System Using Radar and Other Data. *Preprints, 27th Conf. on WAF and 23rd Conf. on NWP*, Chicago, IL, 2 July 2015.

Gao, J., M. Xue, K. Brewster, and K. K. Droegemeier, 2004: A three-dimensional variational data analysis method with recursive filter for Doppler radars. *J. Atmos. Oceanic Tech.*, 21, 457-469.

Hong, S.-Y., and J.-O. J. Lim, 2006: The WRF single-moment 6-class microphysics scheme (WSM6). *J. Korean Meteor. Soc.*, 42, 129–151.

Hu, M., M. Xue, and K. Brewster, 2006: 3DVAR and Cloud Analysis with WSR-88D Level-II Data for the Prediction of the Fort Worth, Texas, Tornadic Thunderstorms. Part I: Cloud Analysis and Its Impact. *Mon. Wea. Rev.*, 134, 675–698.

Hu, M., M. Xue, J. Gao, and K. Brewster, 2006: 3DVAR and Cloud Analysis with WSR-88D Level-II Data for the Prediction of the Fort Worth, Texas, Tornadic Thunderstorms. Part II: Impact of Radial Velocity Analysis via 3DVAR. *Mon. Wea. Rev.*, 134, 699–721.

Kain, J. S., S. J. Weiss, D. R. Bright, M. E. Baldwin, J. J. Levit, G. W. Carbin, C. S. Schwartz, M. L. Weisman, K. K. Droegemeier, D. B. Weber, and K. W. Thomas, 2008: Some Practical Considerations Regarding Horizontal Resolution in the First Generation of Operational Convection-Allowing NWP. *Wea. Forecasting*, 23, 931–952.

Lin, Y.-L., R. D. Farley, and H. D. Orville, 1983: Bulk Parameterization of the Snow Field in a Cloud Model. *J. Climate Appl. Meteor.*, 22, 1065–1092.

McLaughlin, D., D. Pepyne, B. Philips, J. Kurose, M. Zink, E. Knapp, D. Westbrook, E. Lyons, A. Hopf, A. DeFonzo, R. Contreras, T. Djaferis, E. Insanic, S. Frasier, V. Chandrasekar, F. Junyent, N. Bharadwaj, Y. Liu, and Y. Wang, K. Droegemeier, M. Xue, J.

Brotzge, F. Carr, K. Kloesel, K. Brewster, S. Cruz-Pol, and K. Hondl, 2009: Short-Wavelength Technology and the Potential for Distributed Networks of Small Radar Systems, *Bull. Amer. Meteor. Soc.*, 90, 1797-1817.

Milbrandt, J. A. and M. K. Yau, 2005: A Multimoment Bulk Microphysics Parameterization. Part I: Analysis of the Role of the Spectral Shape Parameter. *J. Atmos. Sci.*, 62, 3051–3064.

Milbrandt, J. A. and M. K. Yau, 2005: A Multimoment Bulk Microphysics Parameterization. Part II: A Proposed Three-Moment Closure and Scheme Description. *J. Atmos. Sci.*, 62, 3065–3081.

Noilhan, J. and S. Planton, 1989: A simple parameterization of land surface processes for meteorological models. *Mon. Wea. Rev.*, 117, 536-549.

Potvin, C. K., L. J. Wicker, M. M. French, and D. W. Burgess, 2014: Warn-on-Forecast Sensitivity Experiments with the 19 May 2013 Norman-Shawnee, OK, Tornadic Supercell. *Presentation at 27th Conf. on Severe Local Storms*, Madison, WI, 4 November 2014.

Schenkman A. D., M. Xue, A. Shapiro, K. Brewster, and J. Gao, 2011: Impact of CASA Radar and Oklahoma Mesonet Data Assimilation on the Analysis and Prediction of Tornadic Mesovortices in an MCS. *Mon. Wea. Rev.*, 139, 3422–3445.

Stensrud, D. J., L. J. Wicker, K. E. Kelleher, M. Xue, M. P. Foster, J. T. Schaefer, R. S. Schneider, S. G. Benjamin, S. S. Weygandt, J. T. Ferree, and J. P. Tuell, 2009: Convective-Scale Warn-on-Forecast System. *Bull. Amer. Meteor. Soc.*, 90, 1487–1499.

Stensrud, D. J., L. J. Wicker, M. Xue, D. T. Dawson, N. Yussouf, D. M. Wheatley, T. E. Thompson, N. A. Snook, T. M. Smith, A. D. Schenkman, C. K. Potvin, E. R. Mansell, T. Lei, K. M. Kuhlman, Y. Jung, T. A. Jones, J. Gao, M. C. Coniglio, H. E. Brooks, K. A. Brewster, 2013: Progress and challenges with Warn-on-Forecast. *Atmos. Res.*, 123, 2-16.

Sun, W.-Y., and C.-Z. Chang, 1986: Diffusion model for a convective layer. Part I: numerical 864 simulation of convective boundary layer. *J. Climate App. Meteorol.*, 25, 1445–1453.

Trapp, R. J., and M. L. Weisman, 2003: Low-level mesovortices within squall lines and bow echoes. Part II: Their genesis and implications. *Mon. Wea. Rev.*, 131, 2804–2823.

Xue, M., K. K. Droegemeier, and V. Wong, 2000: The Advanced Regional Prediction System (ARPS) - A multiscale nonhydrostatic atmospheric simulation and prediction tool. Part I: Model dynamics and verification. *Meteor. Atmos. Physics.*, 75, 161-193.

Xue, M., K. K. Droegemeier, V. Wong, A. Shapiro, K. Brewster, F. Carr, D. Weber, Y. Liu, and D.-H. Wang, 2001: The Advanced Regional Prediction System (ARPS) - A multiscale nonhydrostatic atmospheric simulation and prediction tool. Part II: Model physics and applications. *Meteor. Atmos. Physics.*, 76, 134-165.

Xue, M., D.-H. Wang, J.-D. Gao, K. Brewster, and K. K. Droegemeier, 2003: The Advanced Regional Prediction System (ARPS), storm-scale numerical weather prediction and data assimilation. *Meteor. Atmos. Physics*, 82, 139-170.

Xue, M., J. Schleif, F. Kong, K. W. Thomas, Y. Wang, and K. Zhu, 2013: Track and Intensity Forecasting of Hurricanes: Impact of Convection-Permitting Resolution and Global Ensemble Kalman Filter Analysis on 2010 Atlantic Season Forecasts. *Wea. Forecasting*, 28, 1366–1384.

Xue, M., M. Hu, and A. D. Schenkman, 2014: Numerical Prediction of the 8 May 2003 Oklahoma City Tornadic Supercell and Embedded Tornado Using ARPS with the Assimilation of WSR-88D Data. *Wea. Forecasting*, 29, 39–62.

Zalesak, S. T., 1979: Fully Multidimensional Flux-Corrected Transport Algorithms for Fluids. *J. Comput. Phys.*, 31, 335–362.

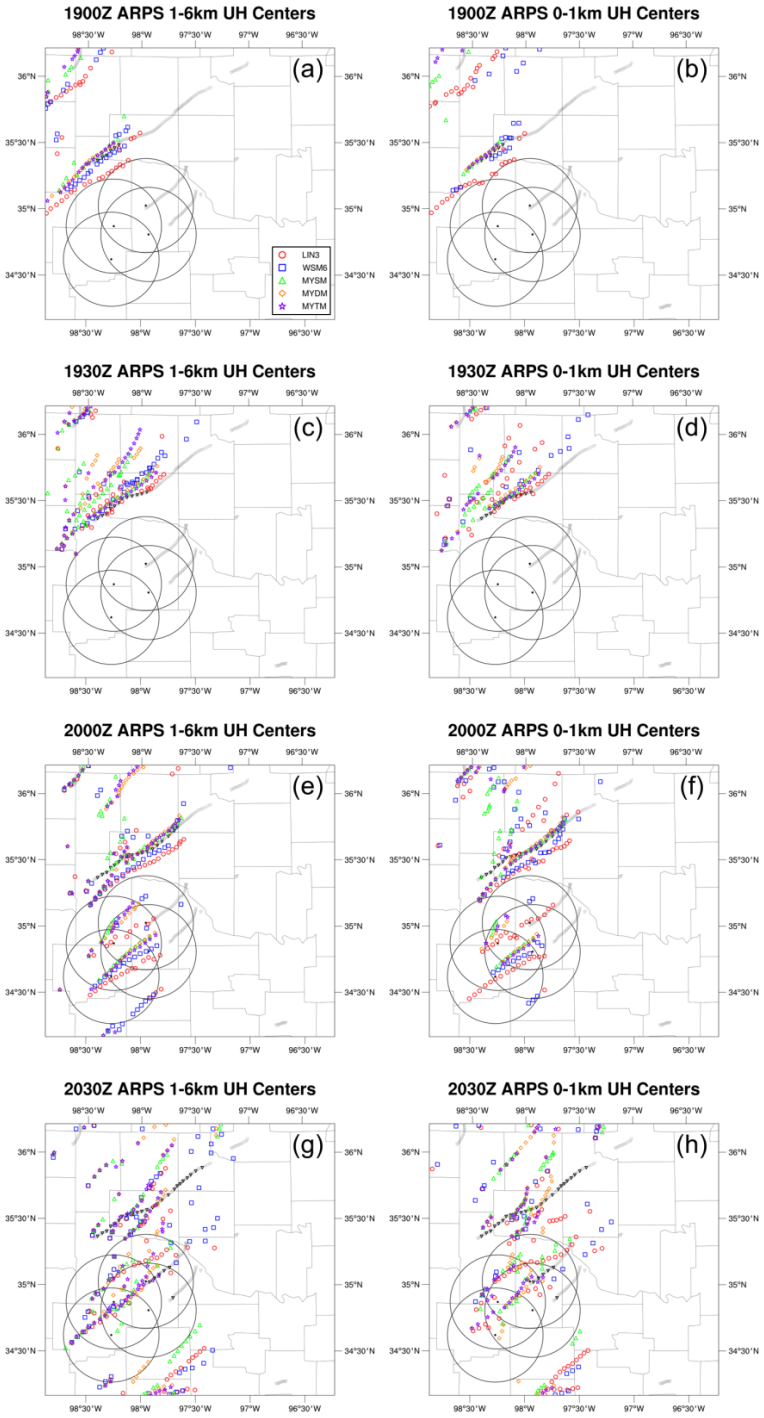
1900Z ARPS 1-6km UH Centers
1900Z ARPS 0-1km UH Centers
1930Z ARPS 1-6km UH Centers
1930Z ARPS 0-1km UH Centers
2000Z ARPS 1-6km UH Centers
2000Z ARPS 0-1km UH Centers
2030Z ARPS 1-6km UH Centers
2030Z ARPS 0-1km UH Centers
(a)
(b)
(c)
(d)
(e)
(f)
(g)
(h)
LIN3
WSM6
MYSM
MYDM
MYTM
98°30'W
98°W
97°30'W
97°W
96°30'W
36°N
35°30'N
35°N
34°30'N

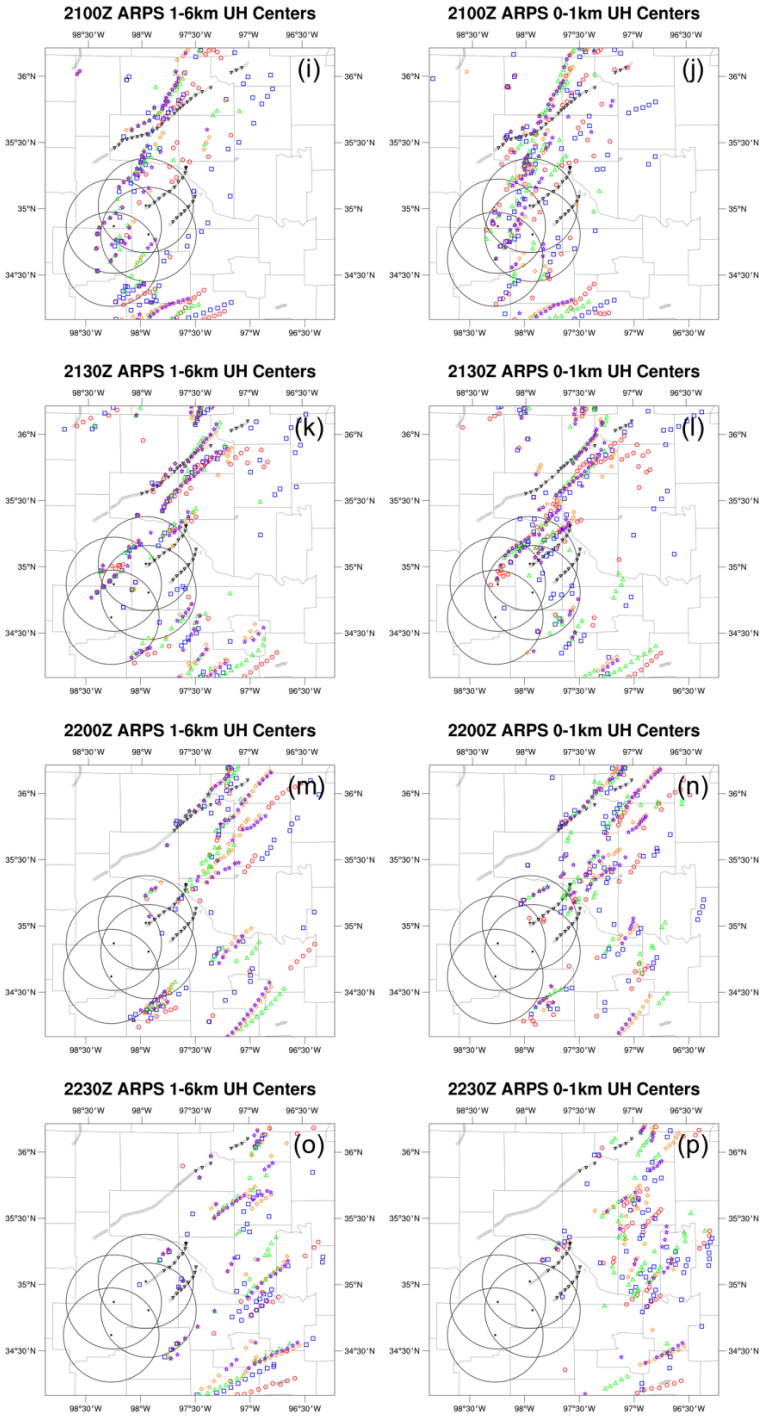

Figure 3. Plots of 1–6-km and 0–1-km UH centers from forecasts every 5 min for each of the simulations. Small grey triangles represent estimated tornado points every 1 min, and small black triangles highlight estimated tornado points used in the ST distance error calculations for each set of simulations. Small black-filled circles represent the locations of the CASA radars, and the larger black circles indicate the 40-km range of the individual CASA radars.

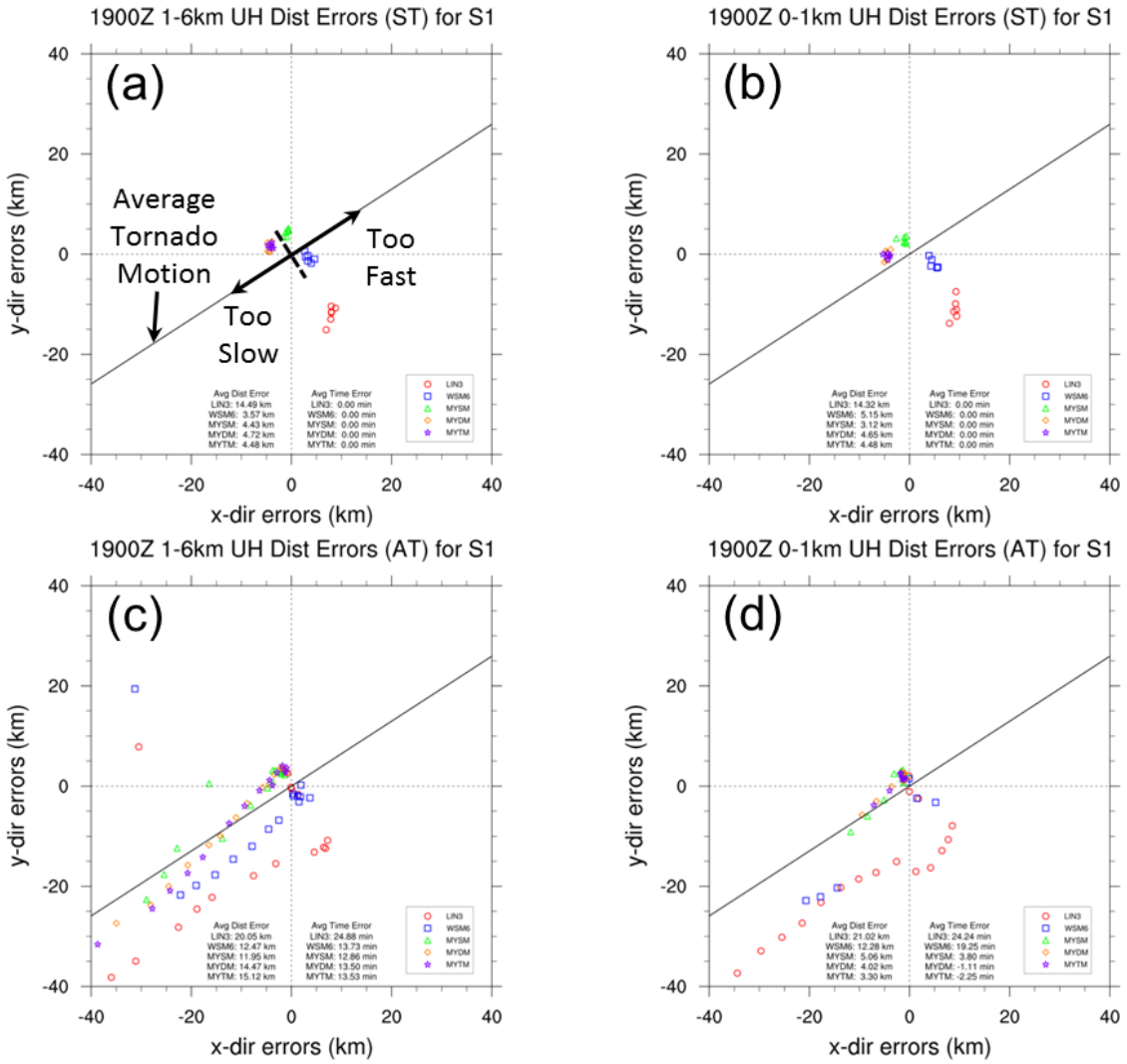

Figure 4. Same-time distance errors between S1's estimated tornado points and (a) 1–6-km UH centers and (b) 0–1-km UH centers from the 1900 UTC simulations. Any-time distance and time errors between S1's estimated tornado points and (c) 1–6-km UH centers and (d) 0–1-km UH centers from the 1900 UTC simulations. For reference, diagonal solid black lines represent the average tornado motions for S1.

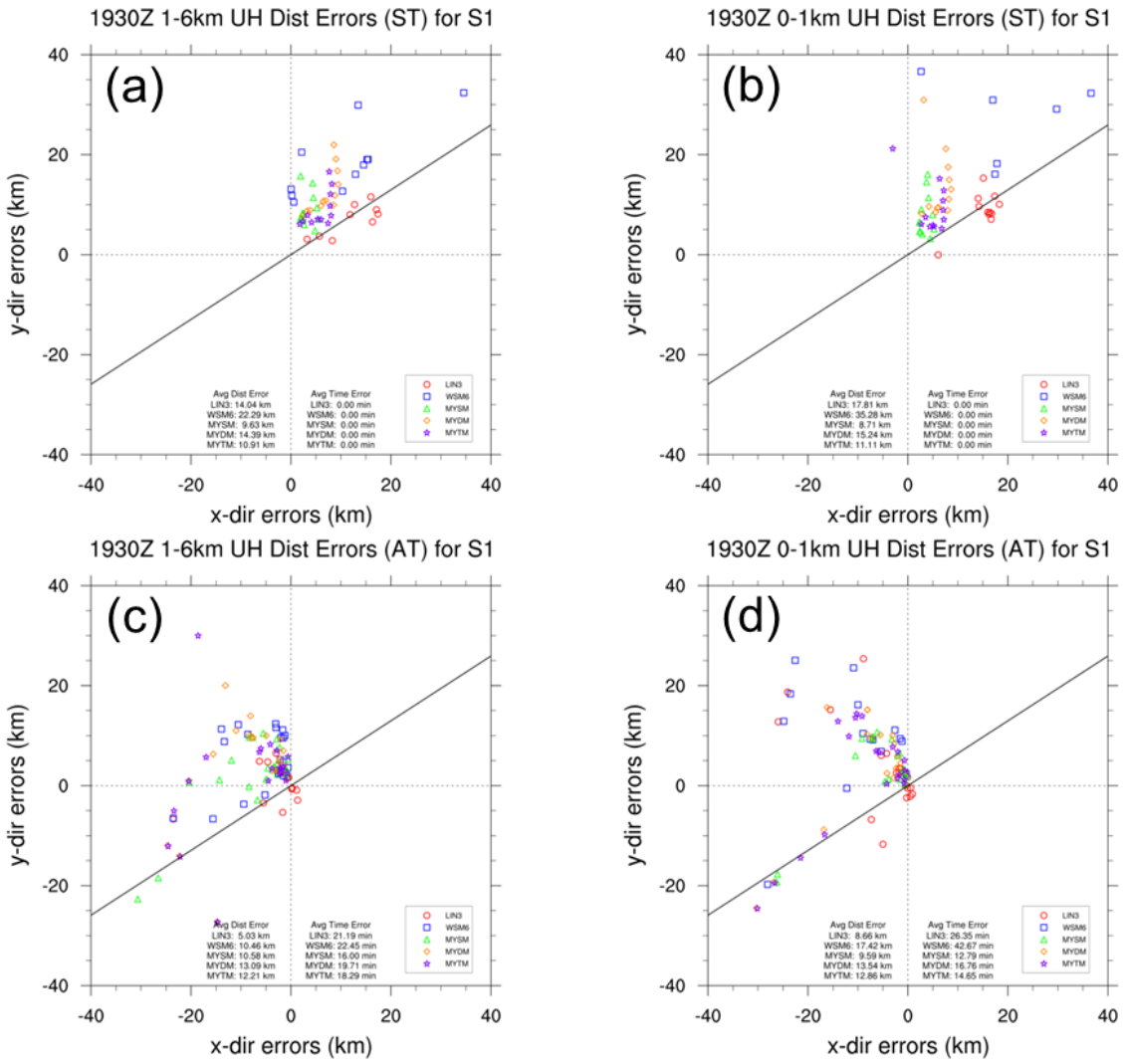

Figure 5. Same as in Fig. 4, but for the 1930 UTC simulations.

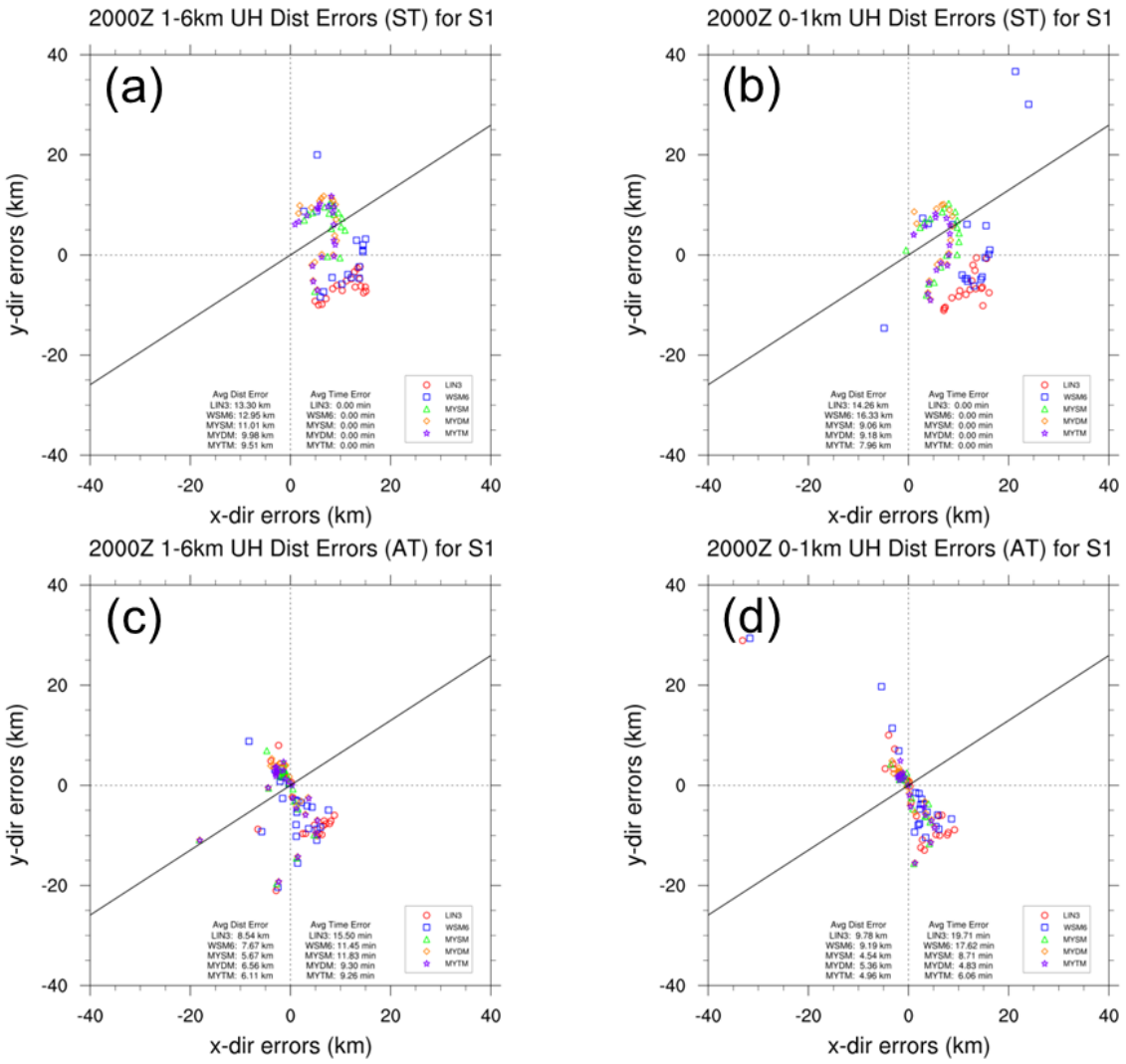

Figure 6. Same as in Fig. 4, but for the 2000 UTC simulations.

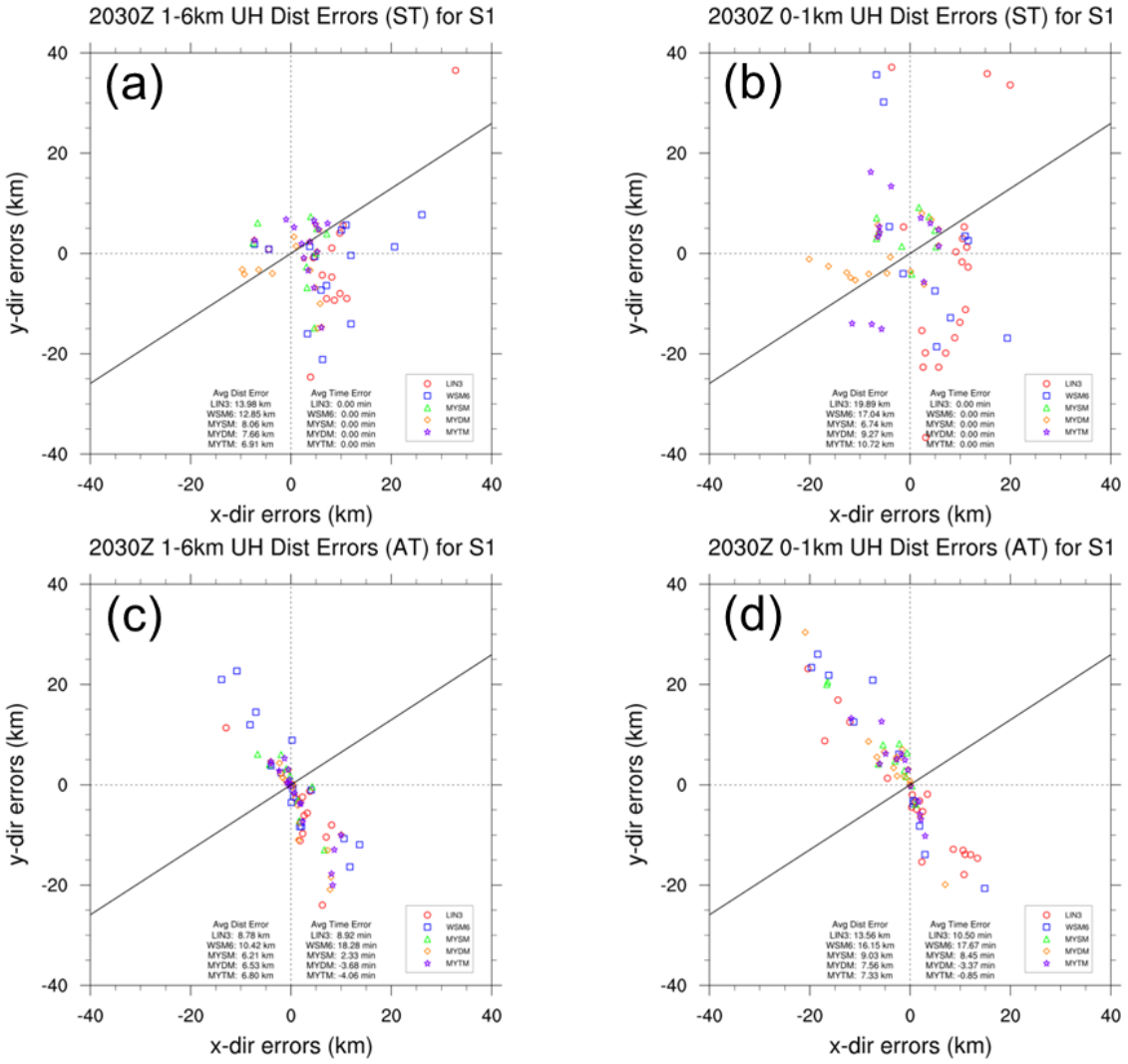

Figure 7. Same as in Fig. 4, but for the 2030 UTC simulations.

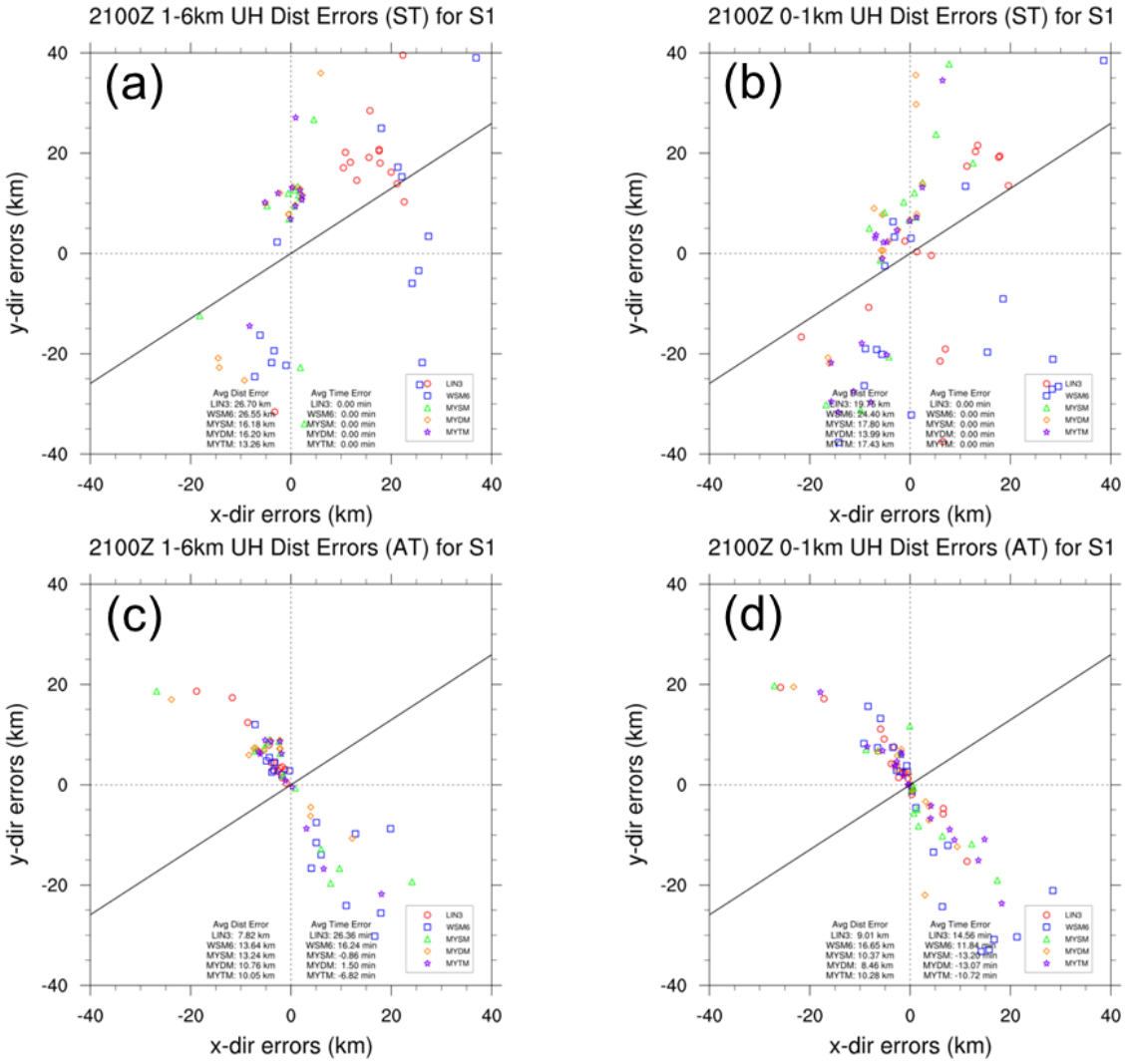

Figure 8. Same as in Fig. 4, but for the 2100 UTC simulations.

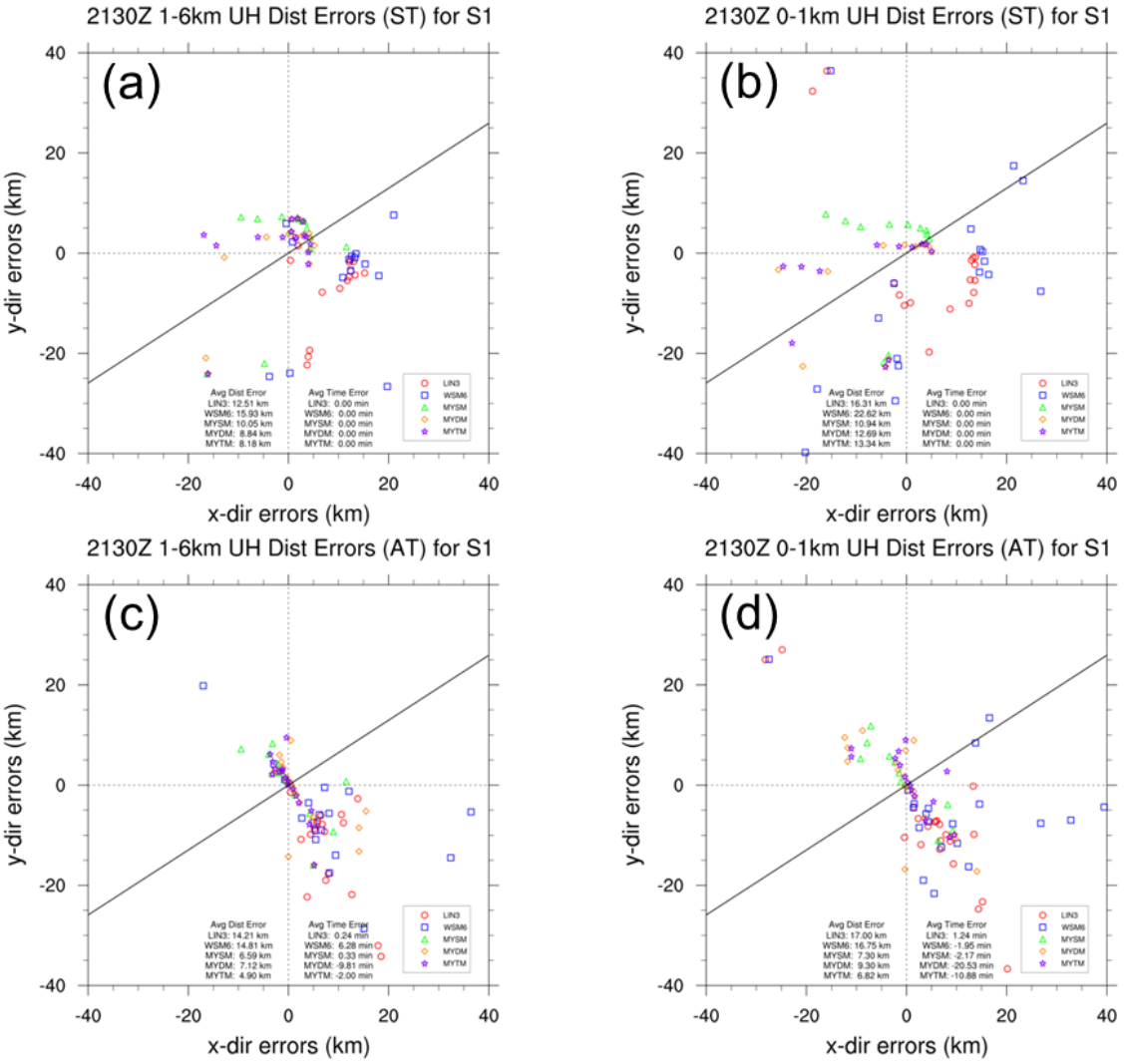

Figure 9. Same as in Fig. 4, but for the 2130 UTC simulations.

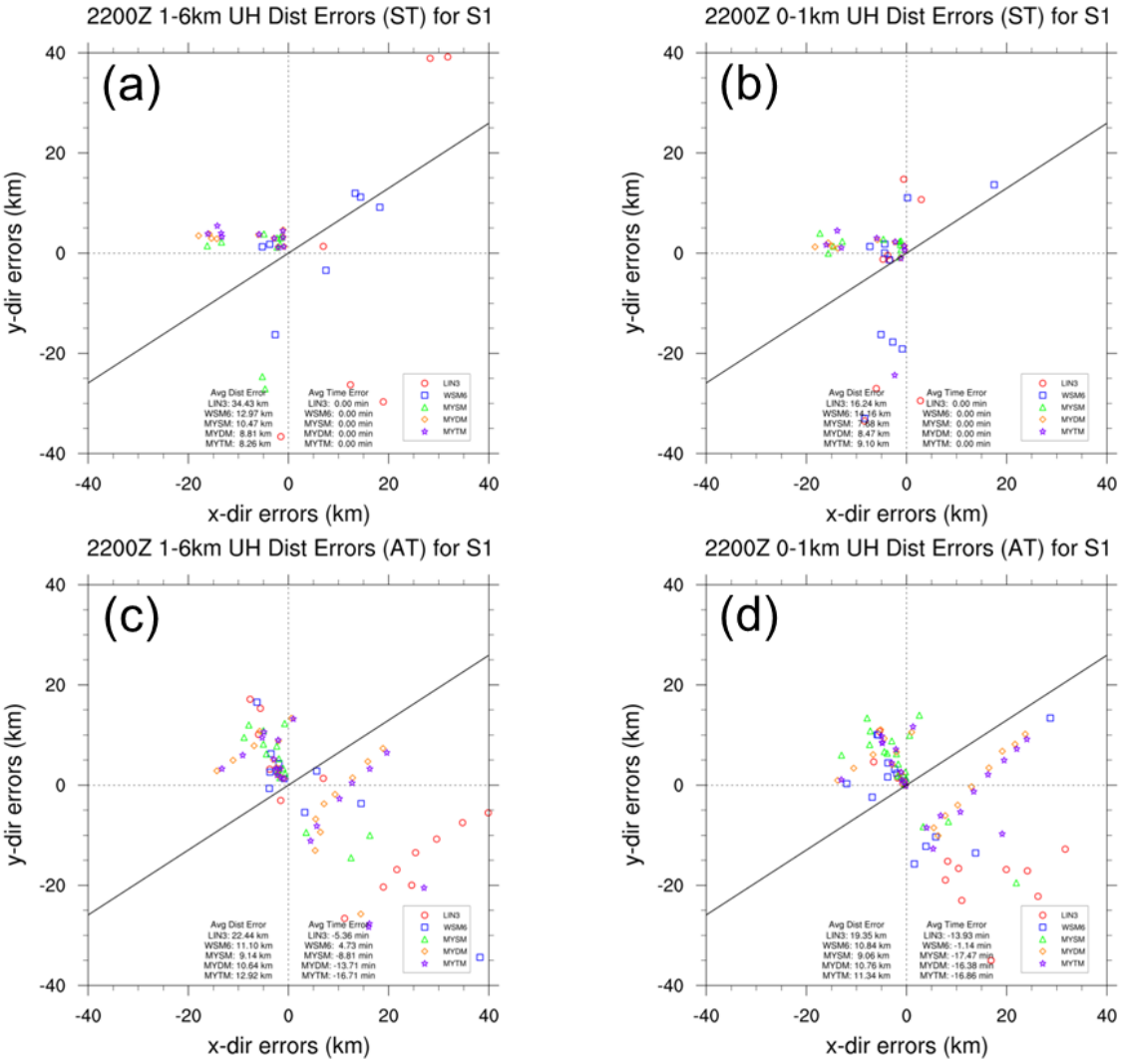

Figure 10. Same as in Fig. 4, but for the 2200 UTC simulations.

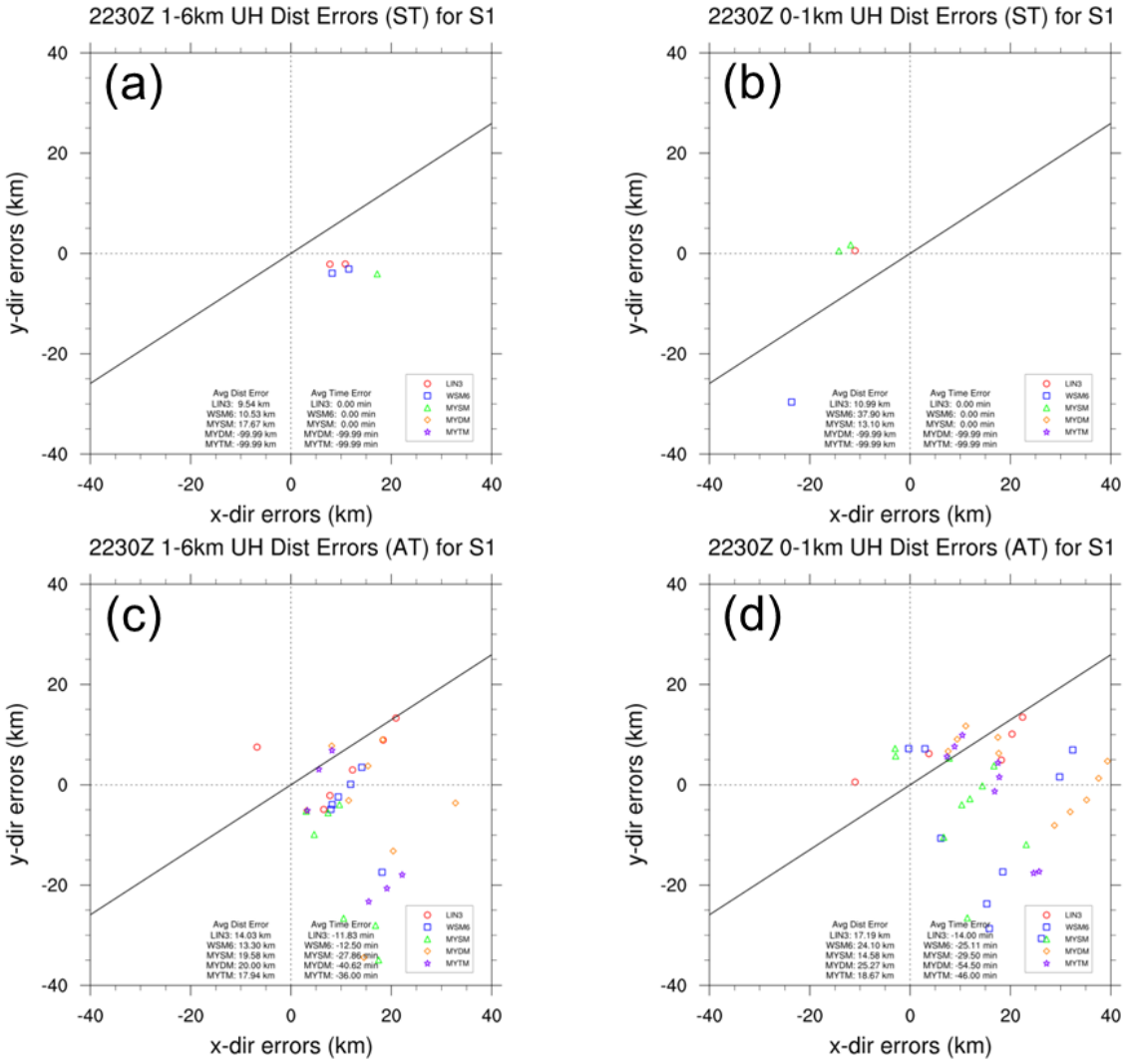

Figure 11. Same as in Fig. 4, but for the 2230 UTC simulations.

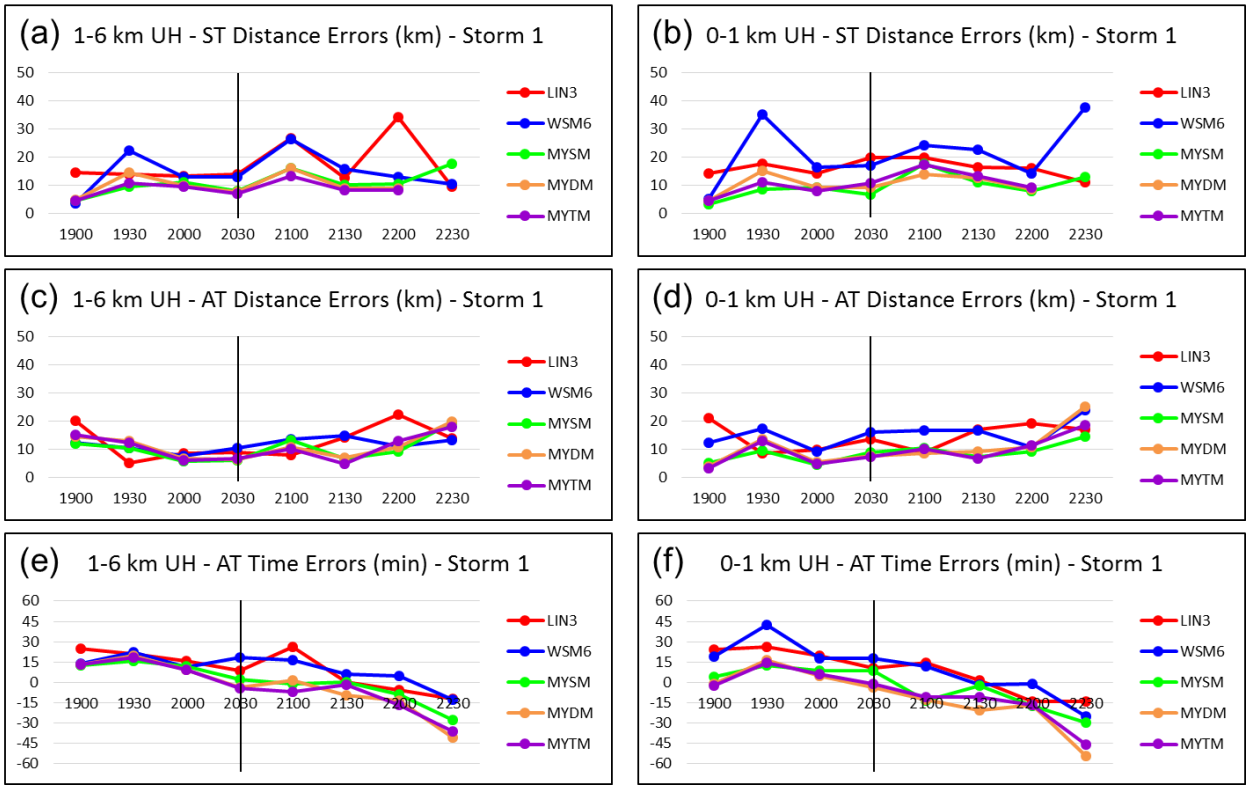

Figure 12. Line graphs of average same-time distance errors (km) between S1's estimated tornado points and (a) 1–6-km UH centers and (b) 0–1-km UH centers from all simulations, average any-time distance errors (km) between S1's estimated tornado points and (c) 1–6-km UH centers and (d) 0–1-km UH centers from all simulations, and average any-time time errors (min) between S1's estimated tornado points and (e) 1–6-km UH centers and (f) 0–1-km UH centers from all simulations. Black vertical lines represent the estimated start time of S1's first tornado.

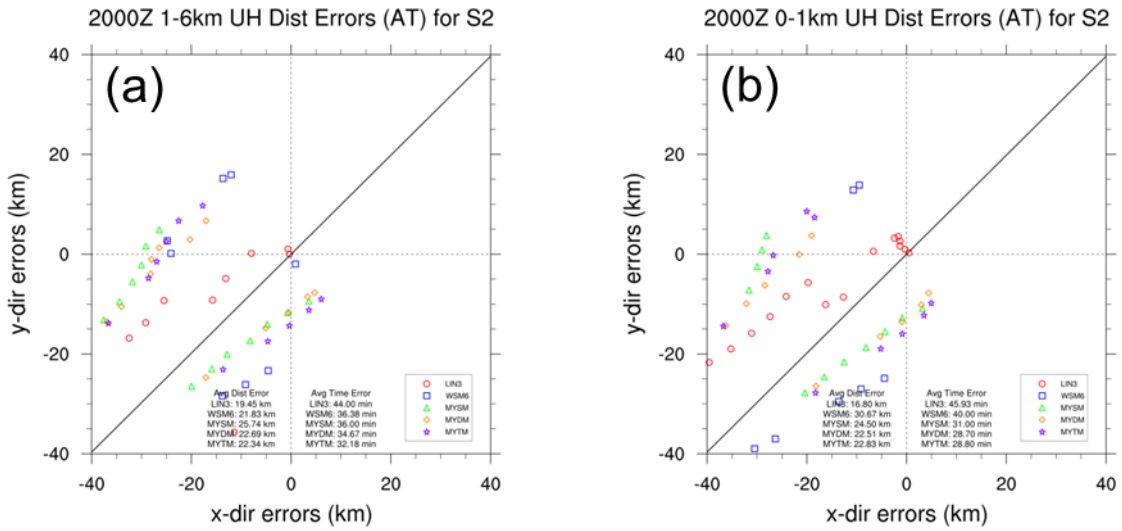

Figure 13. Any-time distance and time errors between estimated tornado points for S2 and (a) 1–6-km UH centers and (b) 0–1-km UH centers from the 2000 UTC simulations. For reference, diagonal solid black lines represent the average tornado motions for S2.

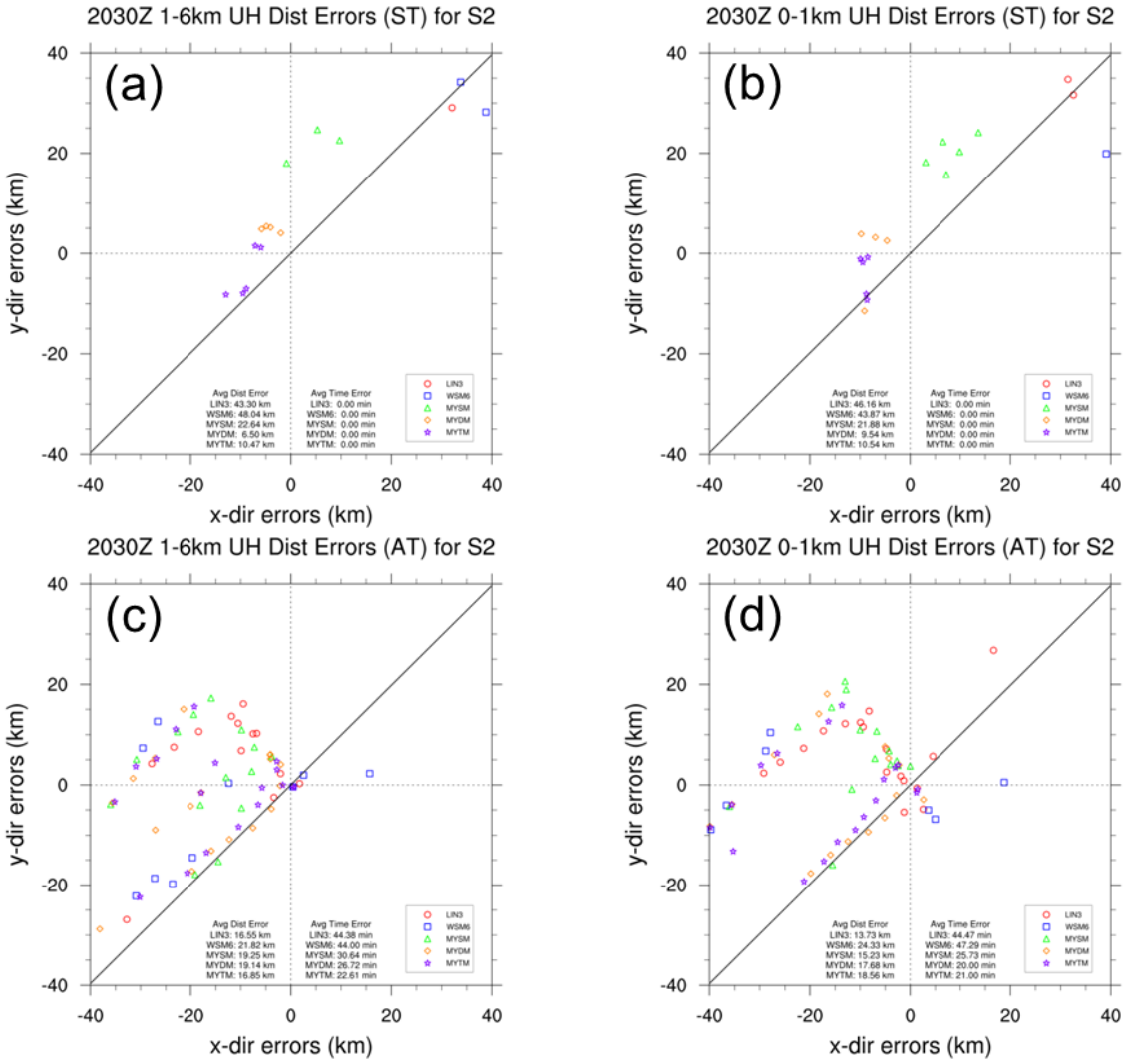

Figure 14. Same-time distance errors between S2's estimated tornado points and (a) 1–6-km UH centers and (b) 0–1-km UH centers from the 2030 UTC simulations. Any-time distance and time errors between S2's estimated tornado points and (c) 1–6-km UH centers and (d) 0–1-km UH centers from the 2030 UTC simulations. For reference, diagonal solid black lines represent the average tornado motions for S2.

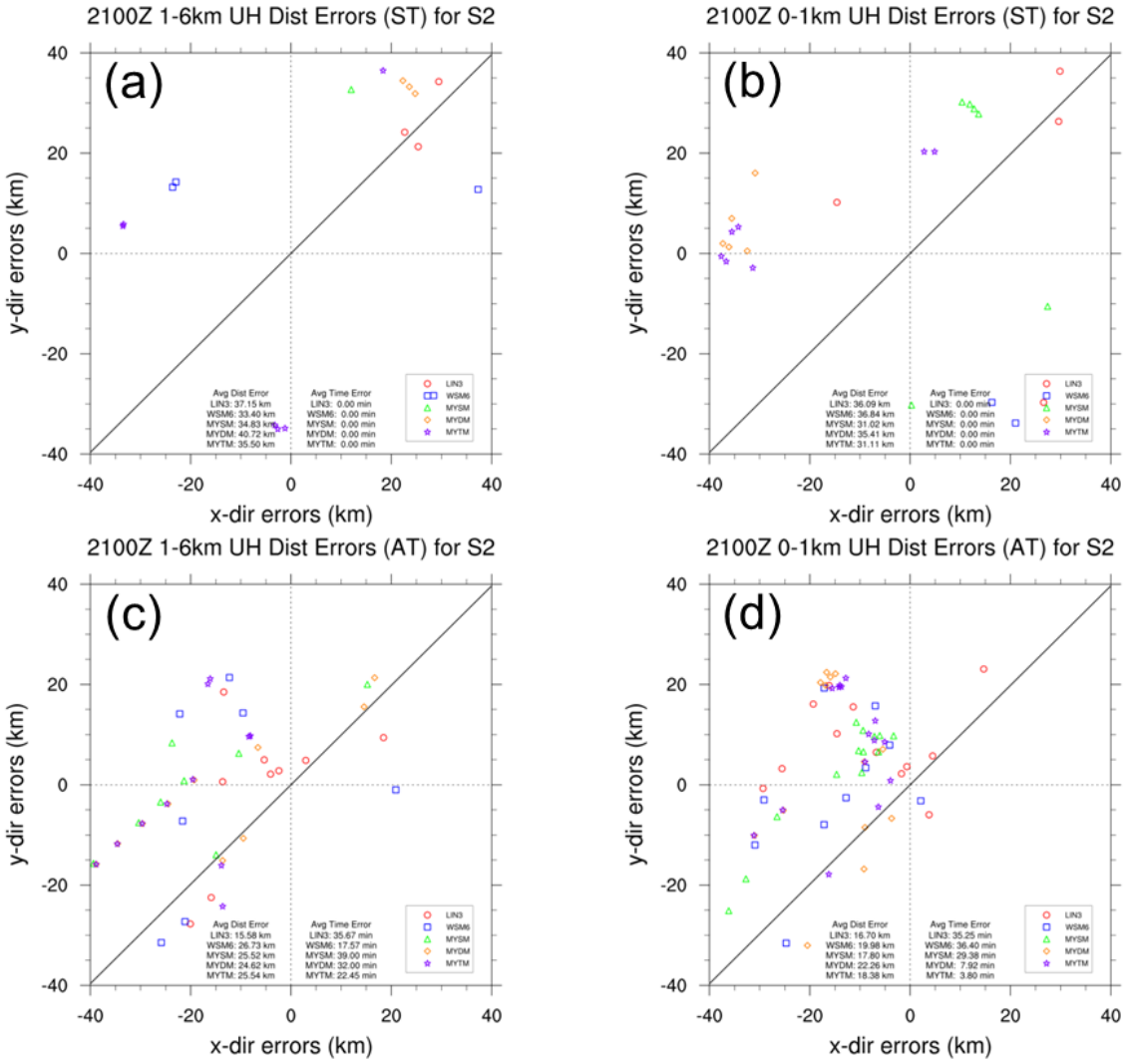

Figure 15. Same as in Fig. 14, but for the 2100 UTC simulations.

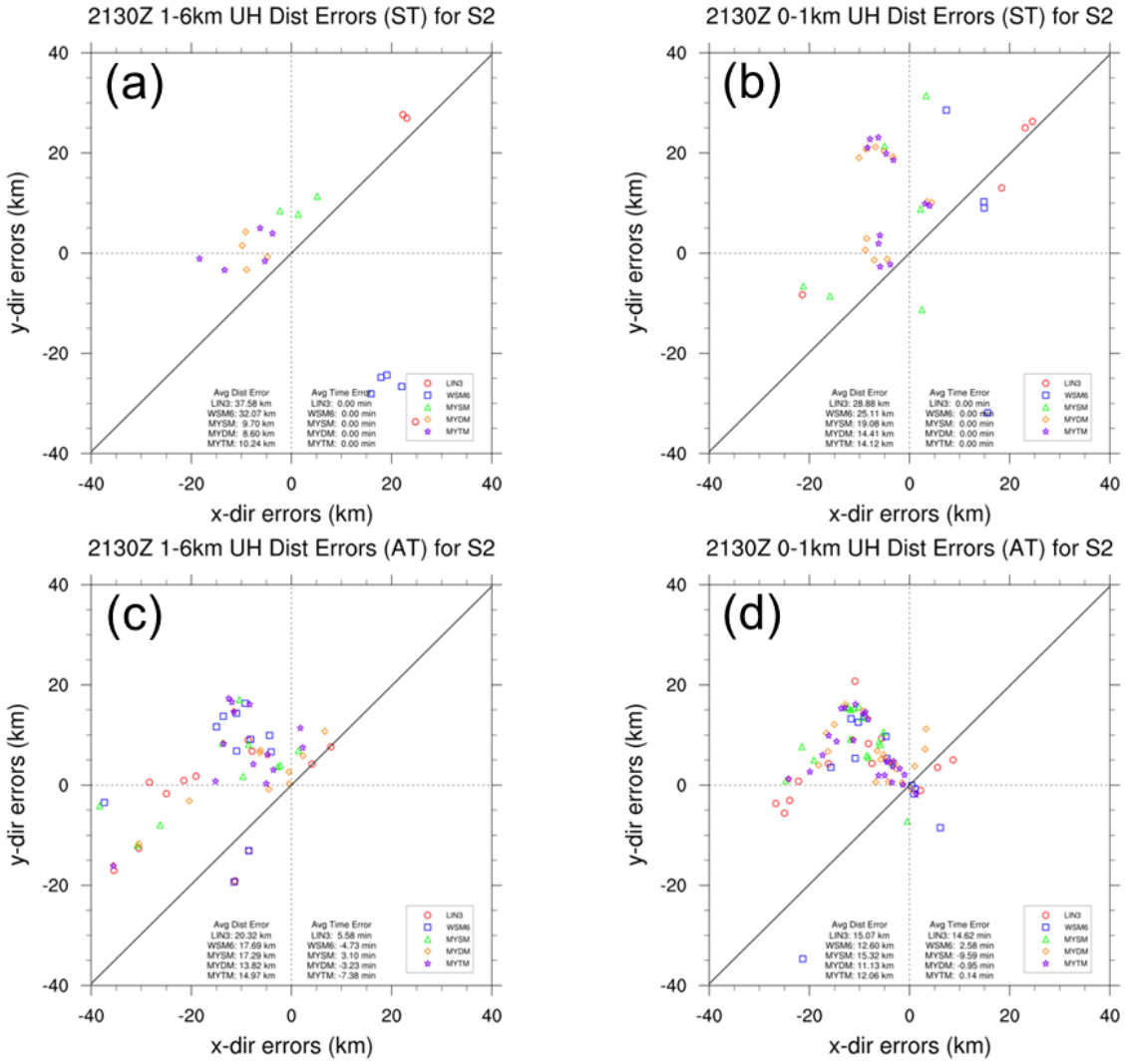

Figure 16. Same as in Fig. 14, but for the 2130 UTC simulations.

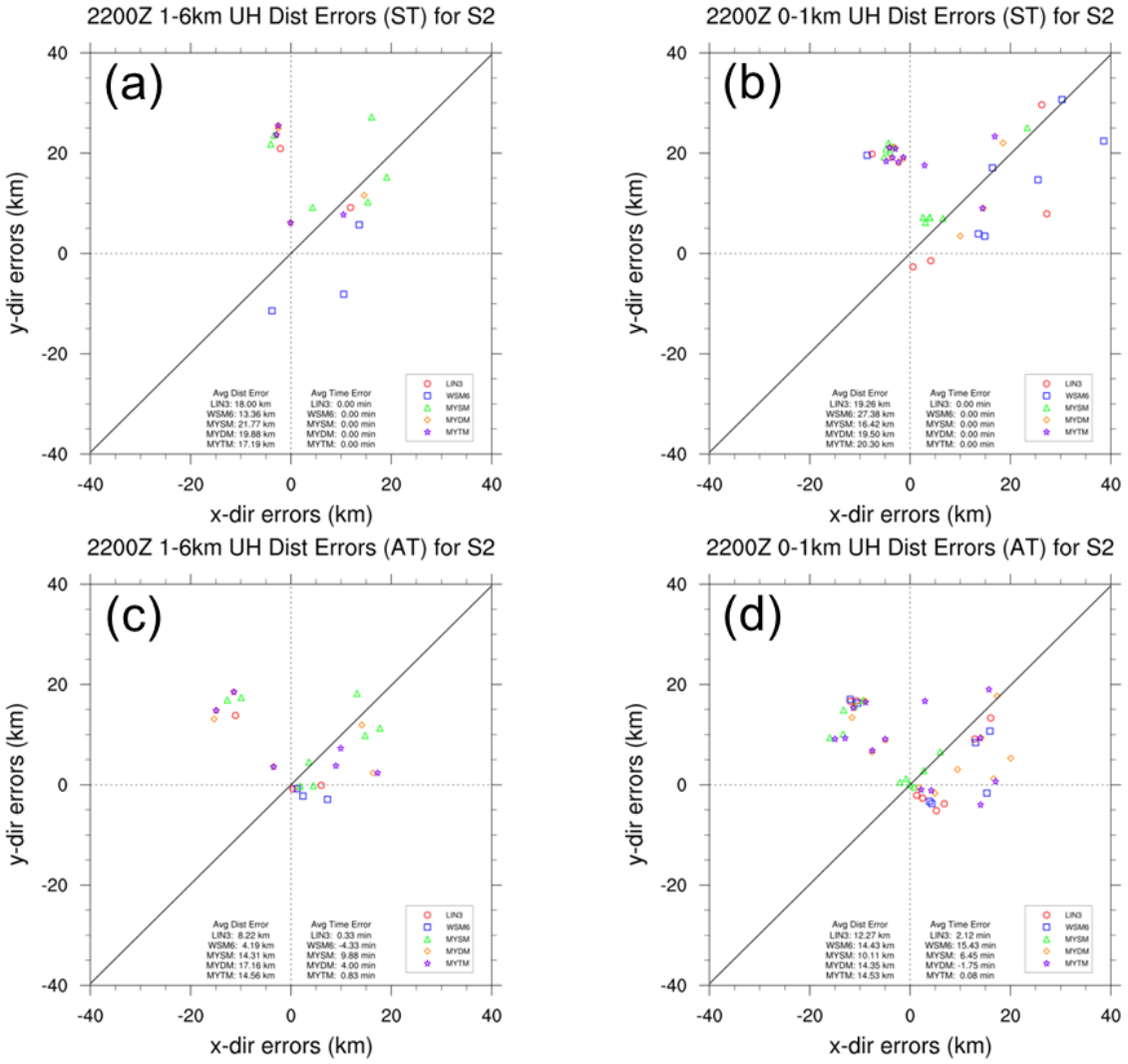

Figure 17. Same as in Fig. 14, but for the 2200 UTC simulations.

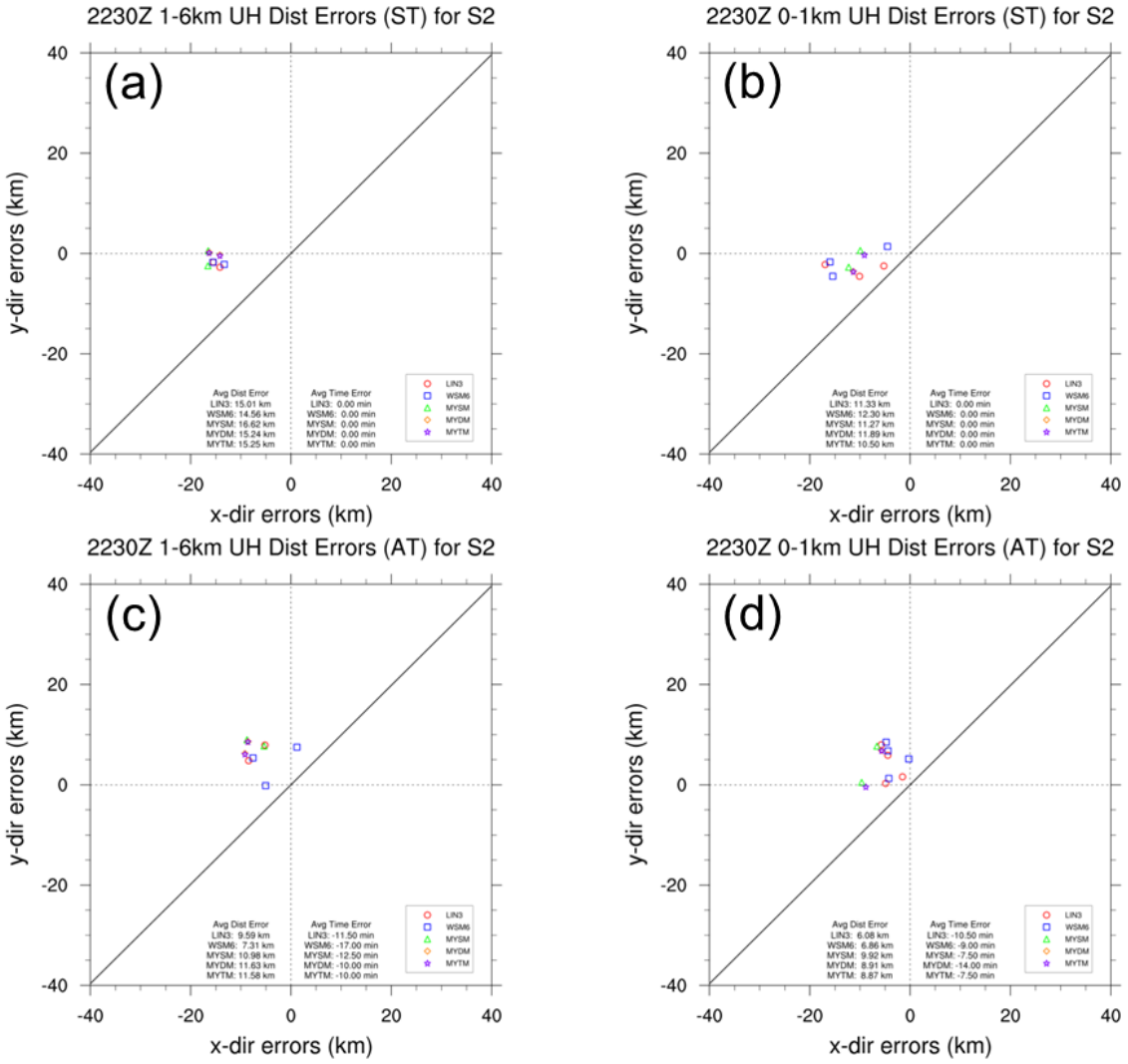

Figure 18. Same as in Fig. 14, but for the 2230 UTC simulations.

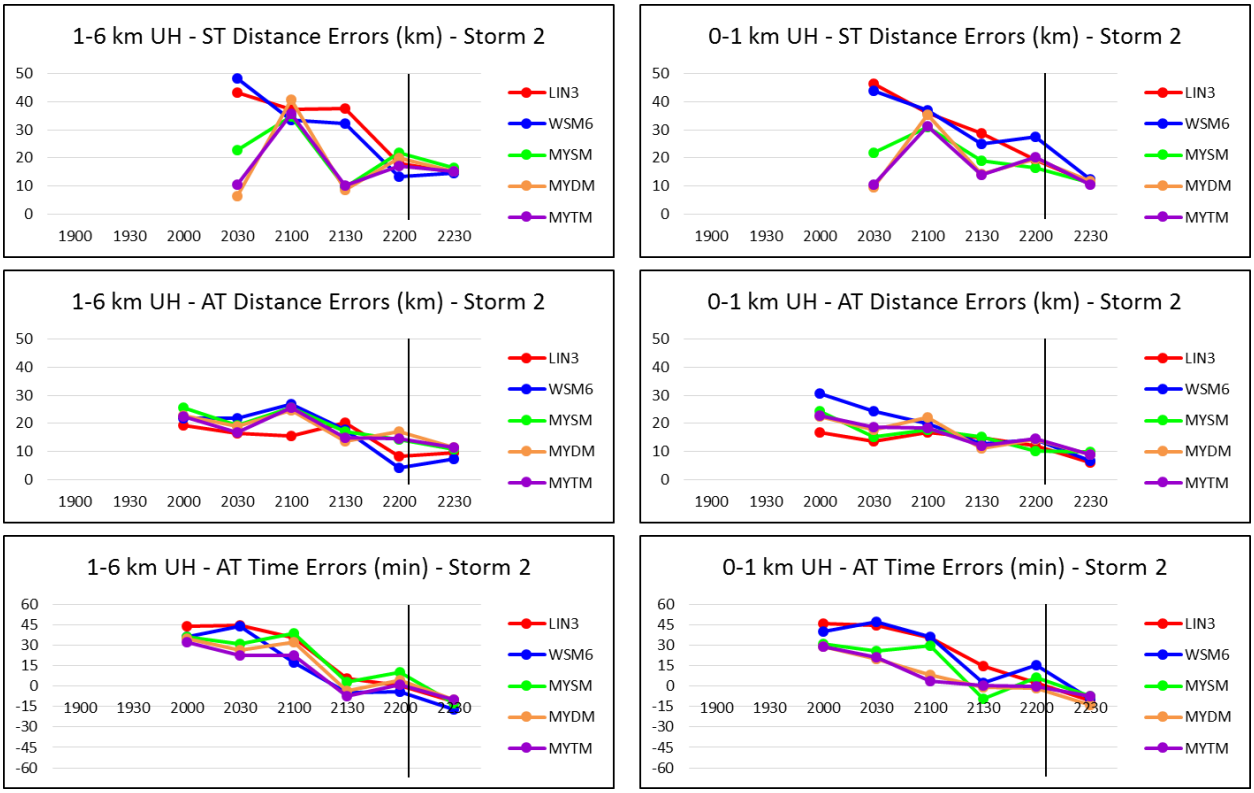

Figure 19. Same as in Fig. 12, but for S2.

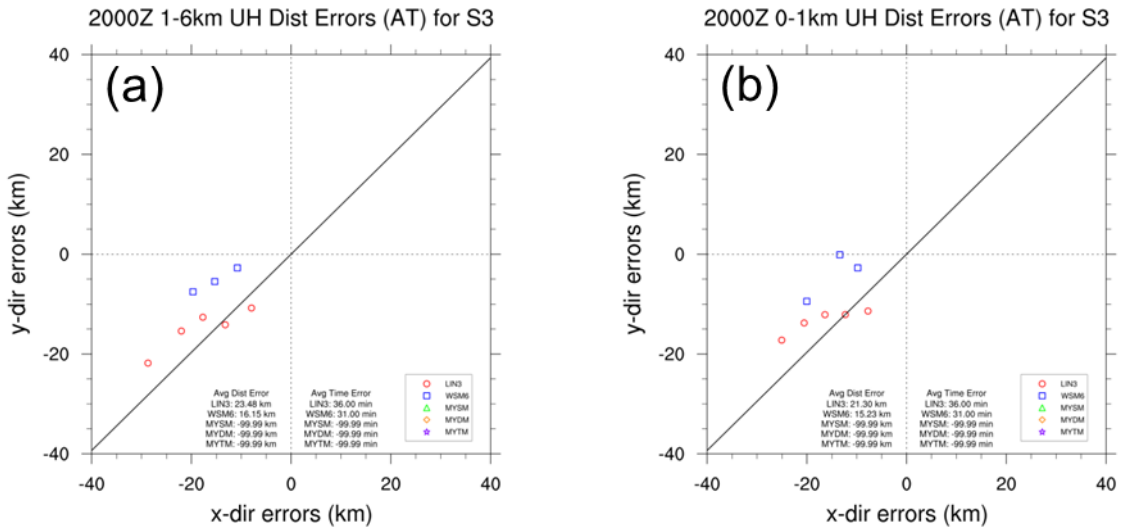

Figure 20. Any-time distance and time errors between S3's estimated tornado points and (a) 1–6-km UH centers and (b) 0–1-km UH centers from the 2000 UTC simulations. For reference, diagonal solid black lines represent the average tornado motions for S3.

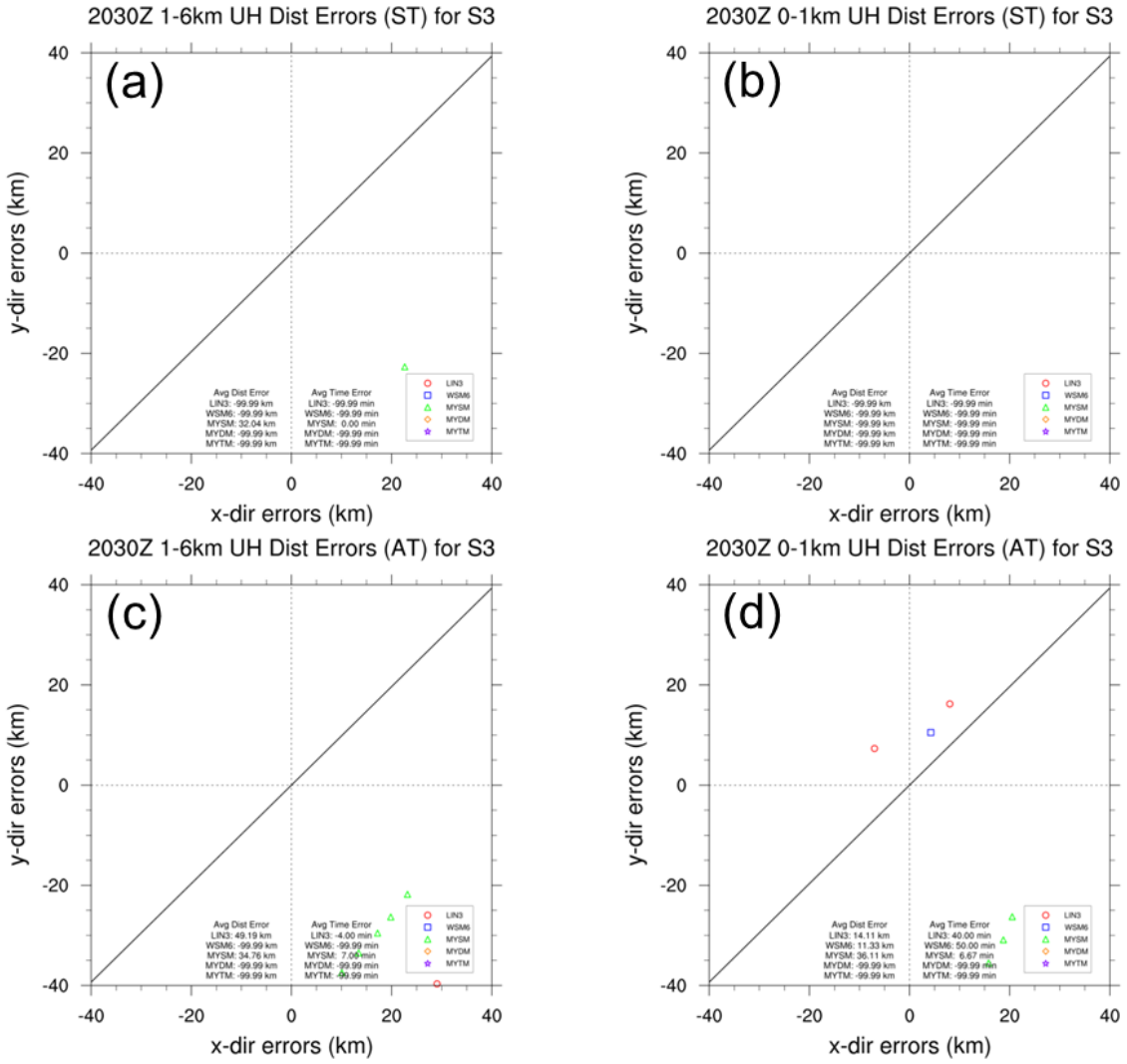

Figure 21. Same-time distance errors between S3's estimated tornado points and (a) 1–6-km UH centers and (b) 0–1-km UH centers from the 2030 UTC simulations. Any-time distance and time errors between S3's estimated tornado points and (c) 1–6-km UH centers and (d) 0–1-km UH centers from the 2030 UTC simulations. For reference, diagonal solid black lines represent the average tornado motions for S3.

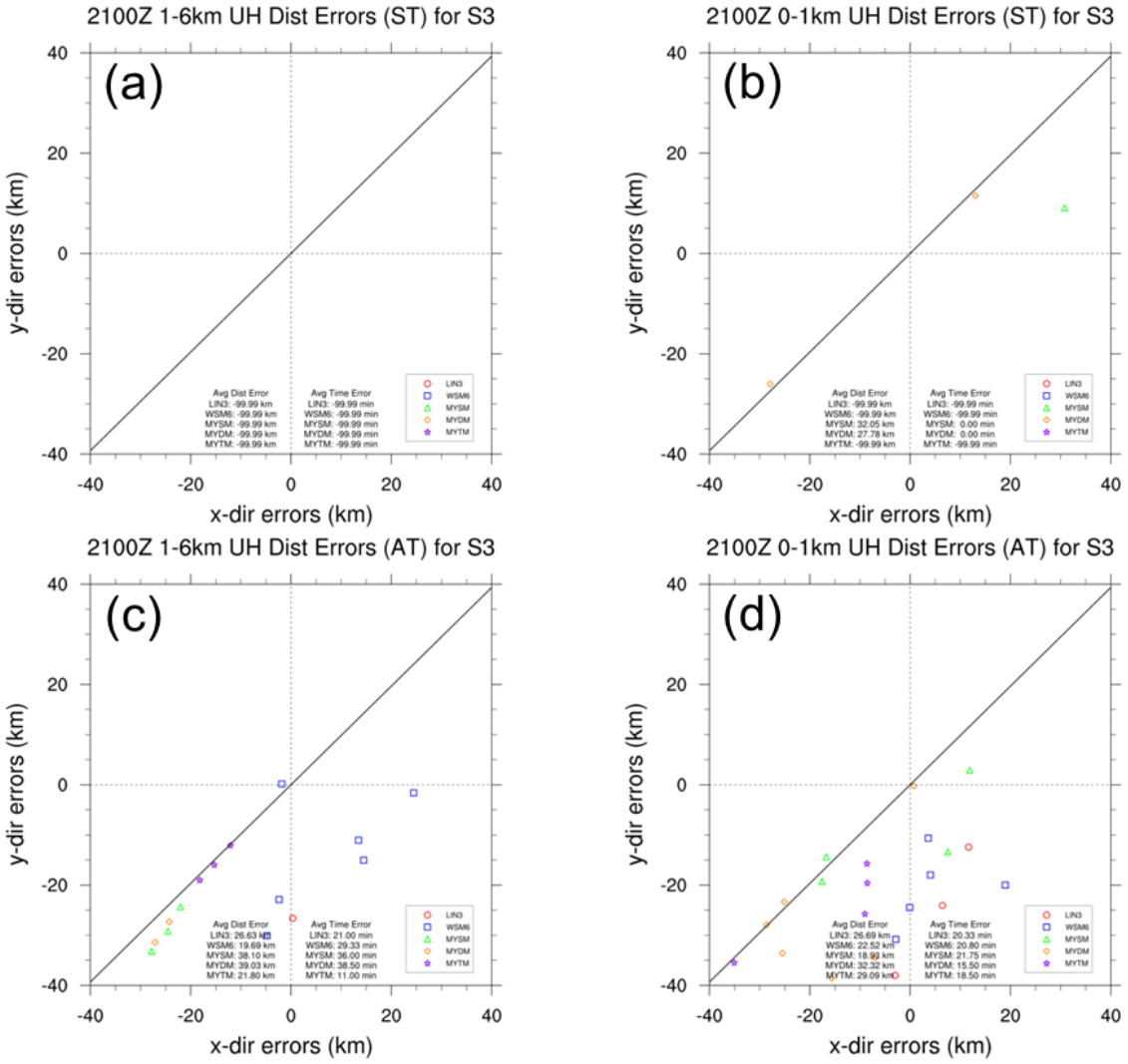

Figure 22. Same as in Fig. 21, but for the 2100 UTC simulations.

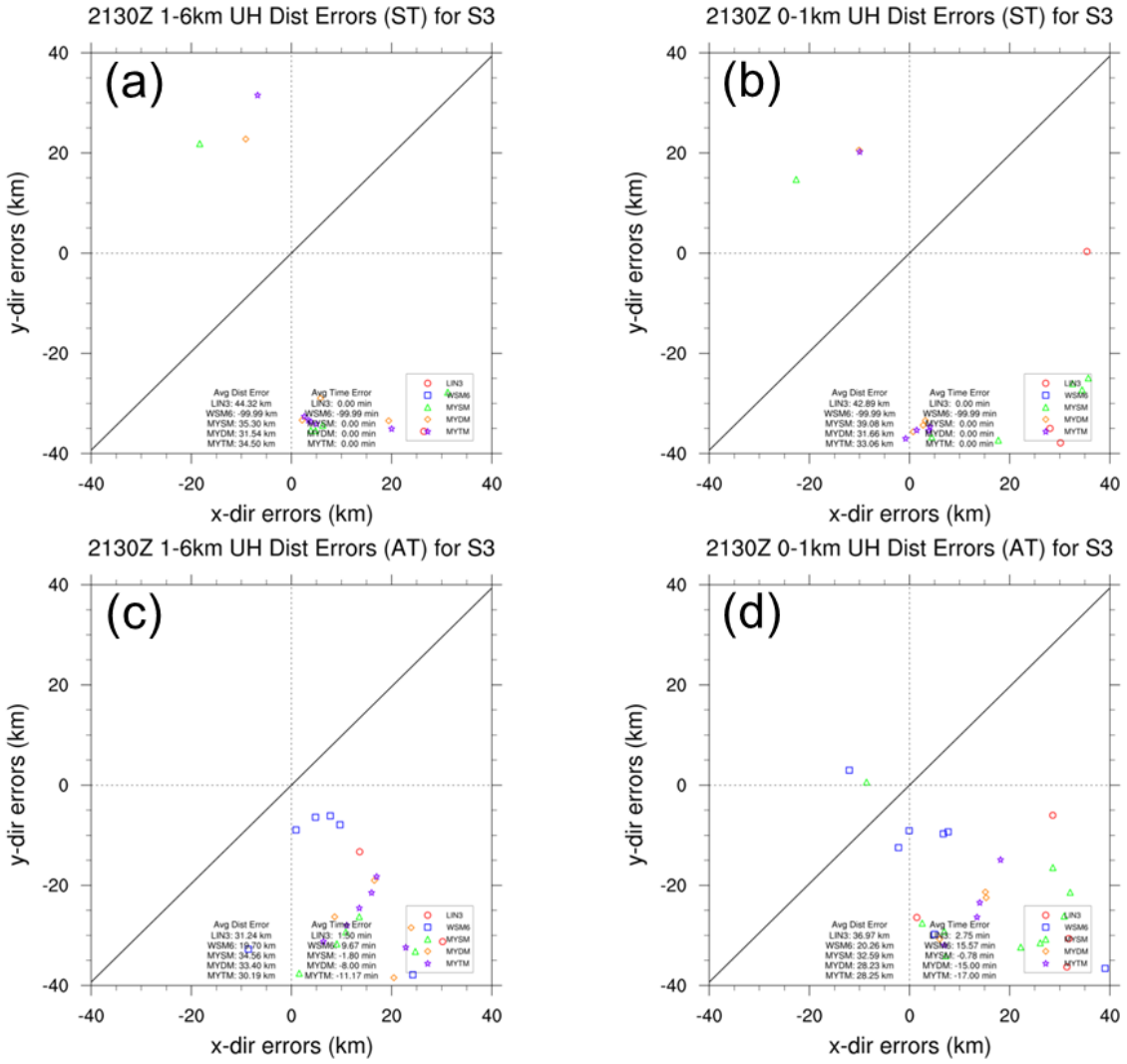

Figure 23. Same as in Fig. 21, but for the 2130 UTC simulations.

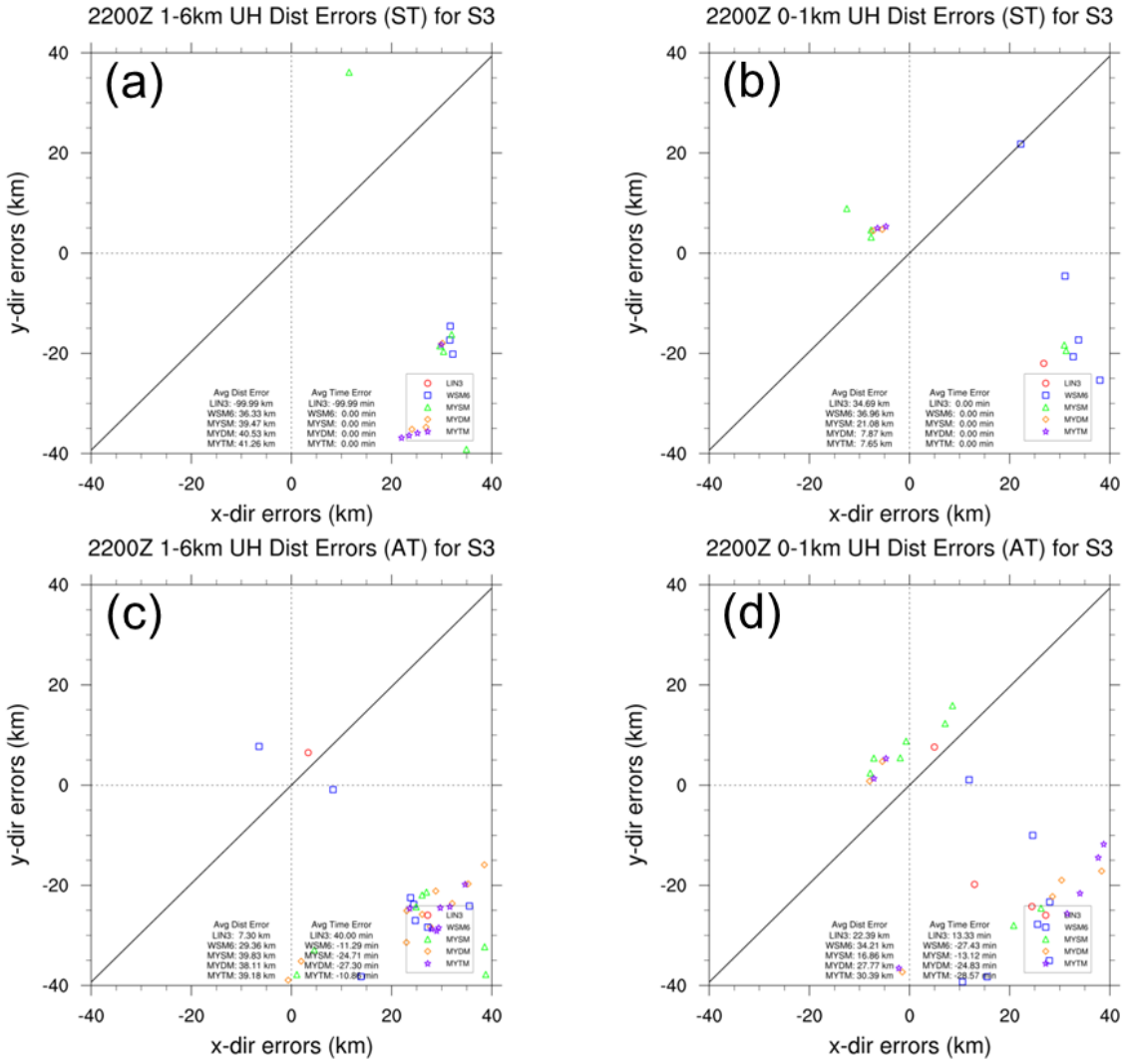

Figure 24. Same as in Fig. 21, but for the 2200 UTC simulations.

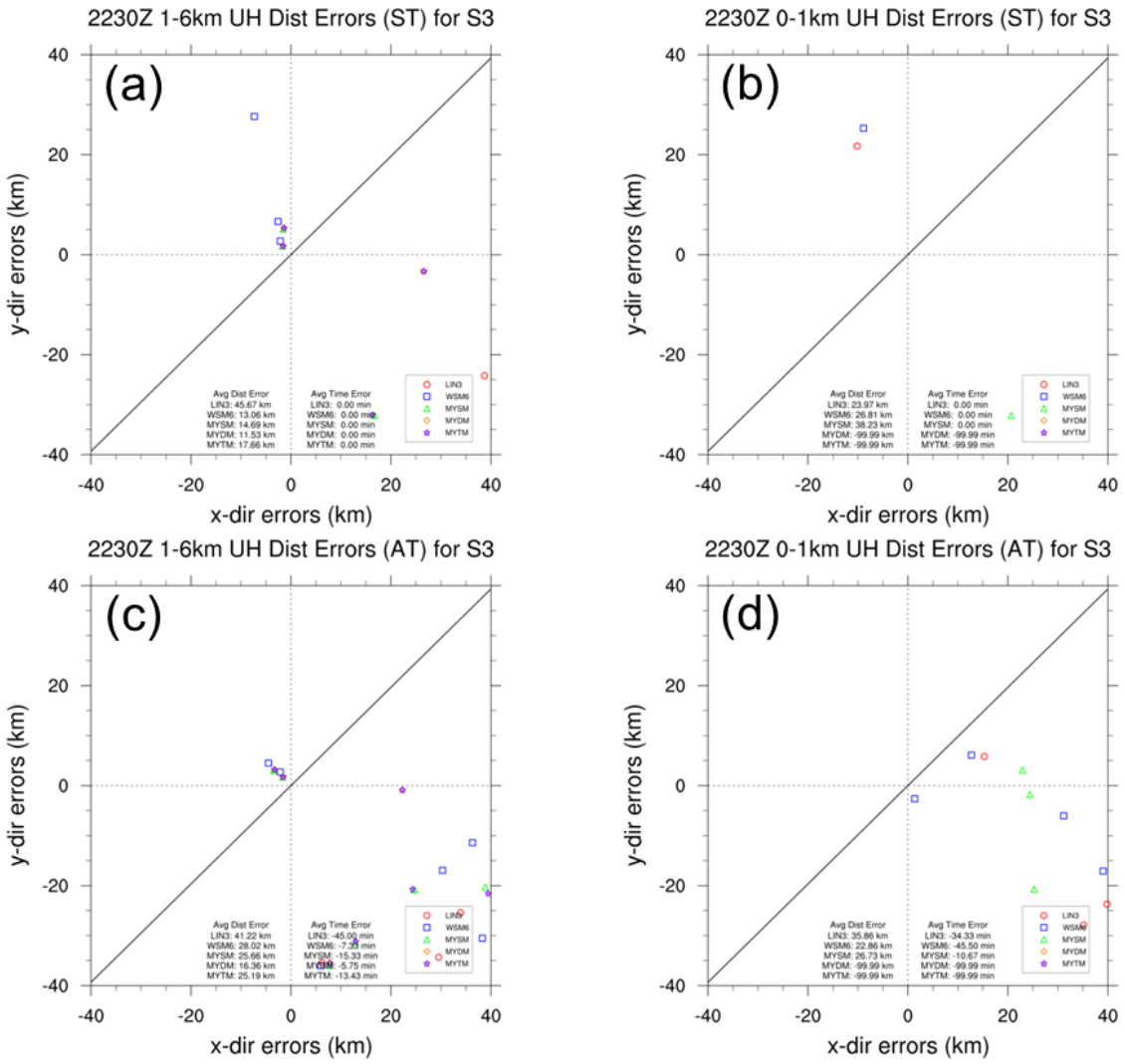

Figure 25. Same as in Fig. 21, but for the 2230 UTC simulations.

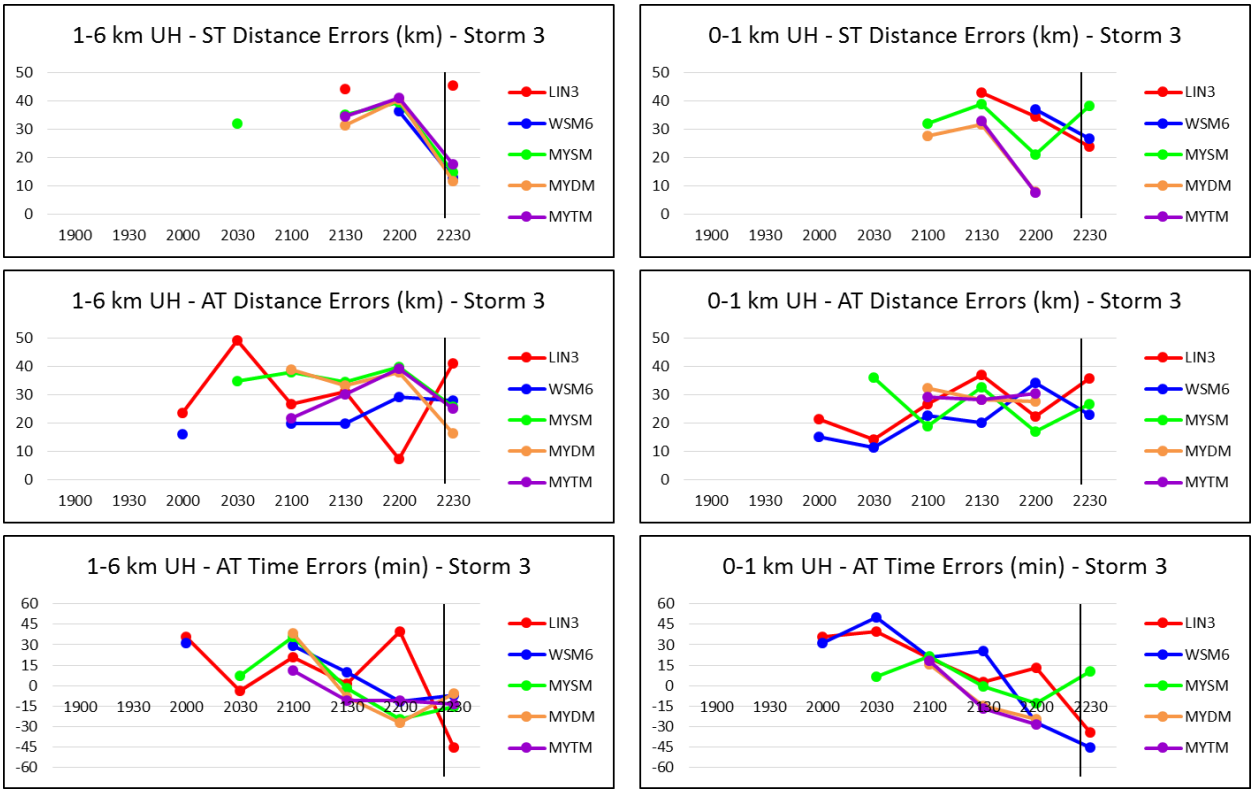

Figure 26. Same as in Fig. 12, but for S3.